J|A|C|S
ARTICLES
Published on Web 02/27/2002

Planar Three-Coordinate High-Spin Fe^{II} Complexes with Large Orbital Angular Momentum: Mössbauer, Electron Paramagnetic Resonance, and Electronic Structure Studies

Hanspeter Andres,[†] Emile L. Bominaar,[†] Jeremy M. Smith,[‡] Nathan A. Eckert,[‡] Patrick L. Holland,*[,‡] and Eckard Münck*[,†]

Contribution from the Departments of Chemistry, Carnegie Mellon University, 4400 Fifth Avenue, Pittsburgh, Pennsylvania 15213, and University of Rochester, Rochester, New York 14627

Received October 10, 2001

Abstract: Mössbauer spectra of $[LFe^{II}X]^0$ (L = β-diketiminate; X = Cl^-, CH_3^-, $NHTol^-$, $NHtBu^-$), **1**.X, were recorded between 4.2 and 200 K in applied magnetic fields up to 8.0 T. A spin Hamiltonian analysis of these data revealed a spin $S = 2$ system with uniaxial magnetization properties, arising from a quasi-degenerate $M_S = \pm 2$ doublet that is separated from the next magnetic sublevels by very large zero-field splittings ($3|D| > 150$ cm^{-1}). The ground levels give rise to positive magnetic hyperfine fields of unprecedented magnitudes, $B_{int} = +82$, $+78$, $+72$, and $+62$ T for **1.**CH_3, **1.**NHTol, **1.**NHtBu, and **1.**Cl, respectively. Parallel-mode EPR measurements at X-band gave effective g values that are considerably larger than the spin-only value 8, namely $g_{eff} = 10.9$ (**1.**Cl) and 11.4 (**1.**CH_3), suggesting the presence of unquenched orbital angular momenta. A qualitative crystal field analysis of g_{eff} shows that these momenta originate from spin−orbit coupling between energetically closely spaced yz and z^2 3d-orbital states at iron and that the spin of the $M_S = \pm 2$ doublet is quantized along x, where x is along the Fe−X vector and z is normal to the molecular plane. A quantitative analysis of g_{eff} provides the magnitude of the crystal field splitting of the lowest two orbitals, $|\epsilon_{yz} - \epsilon_{z^2}| = 452$ (**1.**Cl) and 135 cm^{-1} (**1.**CH_3). A determination of the sign of the crystal field splitting was attempted by analyzing the electric field gradient (EFG) at the ^{57}Fe nuclei, taking into account explicitly the influence of spin−orbit coupling on the valence term and ligand contributions. This analysis, however, led to ambiguous results for the sign of $\epsilon_{yz} - \epsilon_{z^2}$. The ambiguity was resolved by analyzing the splitting Δ of the $M_S = \pm 2$ doublet; $\Delta = 0.3$ cm^{-1} for **1.**Cl and $\Delta = 0.03$ cm^{-1} for **1.**CH_3. This approach showed that z^2 is the ground state in both complexes and that $\epsilon_{xz} - \epsilon_{z^2} \approx 3500$ cm^{-1} for **1.**Cl and 6000 cm^{-1} for **1.**CH_3. The crystal field states and energies were compared with the results obtained from time-dependent density functional theory (TD-DFT). The isomer shifts and electric field gradients in **1.**X exhibit a remarkably strong dependence on ligand X. The ligand contributions to the EFG, denoted W, were expressed by assigning ligand-specific parameters: W_X to ligands X and W_N to the diketiminate nitrogens. The additivity and transferability hypotheses underlying this model were confirmed by DFT calculations. The analysis of the EFG data for **1.**X yields the ordering $W_{N(diketiminate)} < W_{Cl} < W_{N'HR}$, W_{CH_3} and indicates that the diketiminate nitrogens perturb the iron wave function to a considerably lesser extent than the monodentate nitrogen donors do. Finally, our study of these synthetic model complexes suggests an explanation for the unusual values for the electric hyperfine parameters of the iron sites in the Fe−Mo cofactor of nitrogenase in the M^N state.

Introduction

Research aimed at understanding the chemical and biochemical processes that make up the global nitrogen cycle is intensively pursued in many laboratories. The reduction of dinitrogen to ammonia especially has been scrutinized for many decades because it is often the limiting step in nitrogen assimilation by plants and animals.[1] Biological N_2 reduction is brought about by microbes that use the enzyme system nitrogenase. The N_2 reduction site of nitrogenase, the iron−molybdenum cofactor (FeMoco), has been investigated with many chemical, biochemical, and spectroscopic techniques, and the X-ray structure of the cofactor has been reported for the proteins from three organisms.[2] Particularly surprising was the discovery that six of the seven iron sites that constitute the FeMoco have a trigonal sulfido coordination. Three-coordinate

* To whom correspondence should be addressed. E-mail: (P.H.) holland@chem.rochester.edu; (E.M.) em40@andrew.cmu.edu.
[†] Carnegie Mellon University.
[‡] University of Rochester.

(1) Postgate, J. *Nitrogen Fixation*, 2nd ed.; Edward Arnold: Baltimore, 1987.

(2) (a) Chan, M. K.; Kim, J.; Rees, D. C. *Science* **1993**, *260*, 792−794. (b) Kim, J.; Rees, D. C. *Science* **1992**, *257*, 1677−1682. (c) Kim, J.; Rees, D. C. *Nature* **1992**, *360*, 553−560. (d) Peters, J. W.; Stowell, M. H. B.; Soltis, S. M.; Finnegan, M. G.; Johnson, M. K.; Rees, D. C. *Biochemistry* **1997**, *36*, 1181−1187. (e) Kim, J.; Woo, D.; Rees, D. C. *Biochemistry* **1993**, *32*, 7104−7115. (f) Mayer, S. M.; Lawson, D. M.; Gormal, C. A.; Roe, S. M.; Smith, B. E. *J. Mol. Biol.* **1999**, *292*, 871−891.

10.1021/ja012327l CCC: $22.00

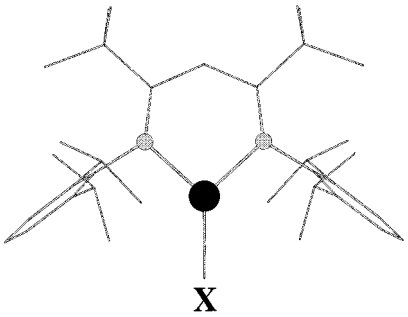

Figure 1. View of the structure of **1**.X along the axis perpendicular to the FeNN plane. The iron and nitrogen atoms are shown as black and grey circles, respectively. The hydrogen atoms are omitted for clarity.

iron is rare in synthetic chemistry,[3] so efforts to expand the database of such compounds are expected to be useful in refining our understanding of the spectroscopic and biochemical signatures of the FeMoco.

We recently reported a new three-coordinate iron(II) compound that is supported by a bulky β-diketiminate ligand.[4] The terminal chloride ligand can be substituted with other ligands, giving compounds **1.**X (Figure 1) that differ only in the nature of X. Although such compounds are highly sensitive to air and water, their thermal stability enables detailed spectroscopic study, and below are described the first steps toward the elucidation of ligand contributions to the electronic structure of three-coordinate Fe(II).

In addition, we have reported that **1.**Cl reacts with N_2 and reductant to give interesting dimers, $[LFeNNFeL]^{n-}$ ($n = 0$, 2), that contain a bridging N_2 with a substantially weakened N−N bond.[5] With the combination of formal N−N bond reduction and low-coordinate iron, these complexes promise substantial progress in understanding the role of low coordination at iron in N_2 activation. Moreover, the diketiminate nitrogens have a delocalized negative charge, are electron rich, soft, and polarizable,[6] and thus have properties associated with the biological thiolate/sulfide ligands. These similarities suggest that results obtained from the diketiminate model complexes will provide insight into iron−sulfur clusters such as FeMoco. Preliminary Mössbauer and EPR studies of $[LFeNNFeL]^{n-}$ ($n = 0$, 2) indicate that these complexes have novel electronic properties. However, to assess the meaning of the spectral features of these exchange-coupled dimers, it is necessary to understand zero-field splittings, *g*-tensors, isomer shifts, magnetic hyperfine interactions, and electric field gradients (EFGs) of the individual iron atoms. Thus, we have so far focused on understanding **1.**X, the monomeric complexes of similar iron−ligand structure.

In this article, we describe detailed Mössbauer and EPR studies of **1.**Cl and the new compound **1.**CH_3. Our studies revealed magnetic hyperfine fields at the ^{57}Fe nuclei of considerable magnitude. Thus, **1.**CH_3 exhibits an internal field of +82 T, which is 20 T larger than the "extraordinarily large" +62.4 T hyperfine field reported for α-iron(II) octaethyltetraazaporphyrin.[7] Analysis of our data in the framework of a crystal field model revealed that the unusually large hyperfine field of **1.**CH_3 results from mixing of closely spaced z^2 and *yz* d-orbitals by spin−orbit coupling, creating an electronic ground state with nearly the maximum attainable orbital angular momentum. Our analysis also revealed a substantial ligand contribution to the electric field gradient tensor, and moreover, this contribution can be partitioned and assigned to the diketiminate nitrogens and ligand X. The large ligand contribution found here seems to be a feature of planar structures, providing insight into the nature of the rather small quadrupole splittings of the trigonal irons of the nitrogenase cofactor.[8] Finally, we report the results of DFT and TD-DFT quantum chemical calculations which substantiate the major features of the electronic level stucture deduced from the crystal field analysis. However, as the quantum chemical calculations reported in this paper do not incorporate spin−orbit coupling, the unusual magnetic properties of the ground states in **1.**X could only be indirectly assessed by these techniques.

2. Materials and Methods

2.1. Synthesis and Characterization. All compounds were synthesized and handled in an MBraun Labmaster glovebox under an atmosphere of N_2 with <1 ppm of O_2 and H_2O. Solvents were deoxygenated and purified using columns of alumina and deoxygenizer (Glass Contour Co.; pentane, diethyl ether, tetrahydrofuran), distillation from Na/benzophenone (hexamethyldisiloxane, C_6D_6), or activated 4 Å molecular sieves (light mineral oil). Celite was dried under vacuum overnight at 250 °C. Lithium amides were prepared by treating a pentane solution of the corresponding amine with butyllithium and collecting the solid precipitate. The ^{1}H NMR spectra of the new compounds have not been fully assigned; they consisted solely of broad singlets. ^{1}H NMR spectroscopic measurements of magnetic susceptibility used the method of Evans[9] and were corrected for diamagnetism using standard values.[10] Elemental analyses were performed by Desert Analytics (Tucson, AZ).

$LFeCH_3$ (1.CH_3). Methylmagnesium chloride (3.0 M in tetrahydrofuran, 0.04 mL, 0.1 mmol) was added to a solution of **1.**Cl (46 mg, 78 μmol) in diethyl ether (10 mL). The solution turned from red to pale orange. Volatile materials were removed under vacuum, and the residue was extracted with pentane (5 mL) and filtered through Celite. Addition of hexamethyldisiloxane (2 mL) and cooling to −35 °C gave

(3) (a) Bradley, D. C.; Hursthouse, M. B.; Rodesiler, P. F. *Chem. Commun.* **1969**, 14−15. (b) Alyea, E. C.; Bradley, D. C.; Copperthwaite, R. G.; Sales, K. D.; Fitzsimmons, B. W.; Johnson, C. E. *J. Chem. Soc. D* **1970**, 1715−1716. (c) Seidel, W.; Lattermann, K. J. *Z. Anorg. Allg. Chem.* **1982**, *488*, 69−74. (d) Roddick, D. M.; Tilley, T. D.; Rheingold, A. L.; Geib, S. J. *J. Am. Chem. Soc.* **1987**, *109*, 945−946. (e) Power, P. P.; Shoner, S. C. *Angew. Chem.* **1991**, *103*, 308−309. (f) Olmstead, M. M.; Power, P. P.; Shoner, S. C. *Inorg. Chem.* **1991**, *30*, 2547−2551. (g) Bartlett, R. A.; Ellison, J. J.; Power, P. P.; Shoner, S. C. *Inorg. Chem.* **1991**, *30*, 2888−2894. (h) MacDonnell, F. M.; Ruhlandt-Senge, K.; Ellison, J. J.; Holm, R. H.; Power, P. P. *Inorg. Chem.* **1995**, *34*, 1815−1822. (i) Stokes, S. L.; Davis, W. M.; Odom, A. L.; Cummins, C. C. *Organometallics* **1996**, *15*, 4521−4530. (j) Putzer, M. A.; Neumueller, B.; Behnicke, K.; Magull, J. *Chem. Ber.* **1996**, *129*, 715−719. (k) O'Donoghue, M. B.; Zanetti, N. C.; Davis, W. M.; Schrock, R. R. *J. Am. Chem. Soc.* **1997**, *119*, 2753−2754. (l) O'Donoghue, M. B.; Davis, W. M.; Schrock, R. R.; Reiff, W. M. *Inorg. Chem.* **1999**, *38*, 243−252. (m) Siemeling, U.; Vorfeld, U.; Neumann, B.; Stammler, H.-G. *Inorg. Chem.* **2000**, *39*, 5159−5160.
(4) Smith, J. M.; Lachicotte, R. J.; Holland, P. L. *Chem. Commun.* **2001**, 1542−1543.
(5) Smith, J. M.; Lachicotte, R. J.; Pittard, K. A.; Cundari, T. R.; Lukat-Rodgers, G.; Rodgers, K. R.; Holland, P. L. *J. Am. Chem. Soc.* **2001**, *123*, 9222−9223.
(6) Randall, D. W.; DeBeer George, S.; Holland, P. L.; Hedman, B.; Hodgson, K. O.; Tolman, W. B.; Solomon, E. I. *J. Am. Chem. Soc.* **2000**, *122*, 11632−11648.
(7) Reiff, W. M.; Frommen, C. M.; Yee, G. T.; Sellers, S. P. *Inorg. Chem.* **2000**, *39*, 2076−2079.
(8) (a) Zimmermann, R.; Münck, E.; Brill, W. J.; Shah, V. K.; Henzl, M. T.; Rawlings, J.; Orme-Johnson, W. H. *Biochim. Biophys. Acta* **1978**, *537*, 185−207. (b) Huynh, B. H.; Münck, E.; Orme-Johnson, W. H. *Biochim. Biophys. Acta* **1979**, *527*, 192−203. (c) Huynh, B. H.; Henzl, M. T.; Christner, J. A.; Zimmermann, R.; Orme-Johnson, W. H.; Münck, E. *Biochim. Biophys. Acta* **1980**, *623*, 124−138. (d) Yoo, S. J.; Angove, H. C.; Papaefthymiou, V.; Burgess, B. K.; Münck, E. *J. Am. Chem. Soc.* **2000**, *122*, 4926−4936.
(9) (a) Evans, D. F. *J. Chem. Soc.* **1959**, 2003. (b) Schubert, E. M. *J. Chem. Educ.* **1992**, *69*, 62.
(10) Kahn, O. *Molecular Magnetism*; Wiley: New York, 1993.

orange crystals of **1.**CH_3. An additional crop of crystals was collected for a total yield of 36 mg (80% yield). ^{1}H NMR (C_6D_6, 400 MHz): δ 132(1H), 44(18H), −4(4H), −28(12H), −111(2H), −122(4H), −134-(12H). Evans μ_{eff} (C_6D_6, 298 K) = 5.5 ± 0.3 β. FTIR (mineral oil): 3055(w), 1621(w), 1505(s), 1360(s), 1321(s), 1253(m), 1209(s), 1149-(m), 1133(s), 1096(s), 1055(m), 1030(m), 933(m), 889(m), 824(m), 775-(s), 751(s), 669(w) cm^{-1}. UV/vis (Et_2O): 380, 430(sh), 520 nm. Anal. Calcd for $C_{36}H_{56}N_2Fe$: C, 75.50; H, 9.86; N, 4.89. Found: C, 75.42; H, 9.96; N, 4.85.

LFeNHR (R = *p*-tolyl, 1.NHTol; R = *tert*-butyl, 1.NHtBu). A solution of LiNHR (1.8 mmol) in diethyl ether (5 mL) was added to a suspension of **1.**Cl (1.7 mmol) in diethyl ether (15 mL). The reaction mixture rapidly became dark red-brown. The reaction was stirred for 2 h, filtered through Celite, concentrated, and cooled to −35 °C to give red crystals. The connectivity of the compounds was verified via X-ray crystallography.

Data for 1.NHTol. Yield: 68%. ^{1}H NMR (C_6D_6, 400 MHz): δ 122, 96, 94, 37.9, 4.0, 0.1, −25.7, −100, −113, −114. Evans μ_{eff} (C_6D_6, 298 K) = 5.3 ± 0.5 β. FTIR (mineral oil): 3313 cm^{-1}(ν_{N-H}). UV/vis (Et_2O): 436(sh), 480(sh) nm.

Data for 1.NHtBu. Yield: 62%. ^{1}H NMR (C_6D_6, 400 MHz): δ 119, 43, 38, −1.7, −28.3, −29.1, −98.5, −103.8, −122.8. Evans μ_{eff} (C_6D_6, 298 K) = 4.8 ± 0.3 β. FTIR (mineral oil): 3282 cm^{-1} (ν_{N-H}). UV/vis (Et_2O): 512, 561 nm.

X-ray Structural Determination of 1.CH_3. An orange crystal (0.4 × 0.3 × 0.3 mm) was mounted under Paratone-8277 on a glass fiber and placed in a cold nitrogen stream at −80 °C on the X-ray diffractometer. X-ray intensity data were collected on a standard Siemens SMART CCD area detector system equipped with a normal focus Mo-target X-ray tube operated at 2.0 kW (50 kV, 40 mA). A total of 1321 frames of data (1.3 hemispheres) were collected using a narrow frame method with scan widths of 0.3° in ω and exposure times of 10 s/frame using a detector-to-crystal distance of 5.09 cm (maximum 2θ angle of 56.6°). Frames were integrated with the Siemens SAINT program to yield a total of 7348 reflections, of which 2501 were independent (R_{int} = 1.66%). Laue symmetry revealed a monoclinic crystal system, and the final unit cell parameters were determined from the least-squares refinement of three-dimensional centroids of 4546 reflections. The data were corrected for absorption with the SADABS[11] program.

Systematic absences allowed the space group to be assigned as *C*2/c, using the XPREP program (Siemens, SHELXTL,[12] version 5.04). The structure was solved using direct methods and refined employing full-matrix least-squares on F^2 (SHELXTL). All non-hydrogen atoms were refined with anisotropic thermal parameters. Hydrogen atoms were included in idealized positions with riding thermal parameters. The structure refined to a goodness of fit (GOF) of 1.034 and final residuals of R_1 = 2.82% and wR_2 = 7.31% ($I > 2\sigma(I)$).

2.2. Sample Preparation. Mössbauer samples (polycrystalline samples suspended in mineral oil) were transported and analyzed in Delrin cups with tight-fitting lids to avoid exposure of the samples to oxygen. When such lids were not used, sample decomposition was evident, even at low temperatures. Quartz EPR tubes containing polycrystalline samples suspended in mineral oil were flame-sealed under <1 atm N_2.

2.3. Spectroscopic Instrumentation. Mössbauer spectra were collected on constant acceleration spectrometers, which allowed recording spectra between 1.5 and 200 K in fields up to 8.0 T. Isomer shifts are quoted relative to Fe metal at room temperature. The spectra were analyzed using the WMOSS software (WEB Research Co., Edina, MN). EPR spectra were recorded on a BrukerESP 300 equipped with an ESR 910 helium continuous flow cryostat and an Oxford temperature controller. For the analysis of the spectra, we have used software written by Dr. M. P. Hendrich at Carnegie Mellon University.

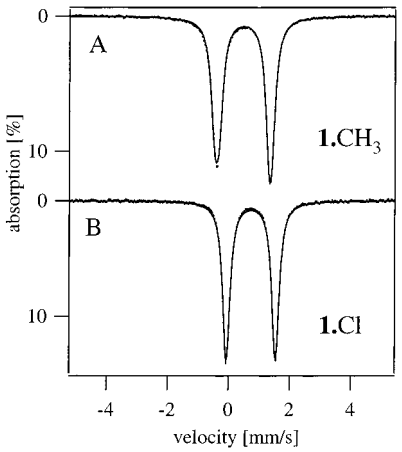

Figure 2. 4.2 K Mössbauer spectra of polycrystalline samples of **1.**CH_3 (A) and **1.**Cl (B) recorded at 4.2 K in zero field. The solid lines are the result of least-squares fitting doublets to the data.

3. Results

3.1. Synthesis and Structure. The synthesis and structure of **1.**Cl were reported recently.[4] It was possible to replace the chloride ligand with other monoanionic ligands through simple metathesis reactions, giving the relatives **1.**CH_3, **1.**NH(*p*-tolyl), and **1.**NH(*tert*-butyl). Proton NMR spectroscopy and magnetic measurements are consistent with a high-spin iron(II) configuration at room temperature. Each of these complexes has been analyzed by X-ray crystallography, in each case revealing a planar three-coordinate geometry of the type shown in Figure 1. The structures of the amidoiron complexes will be described fully at a later time.

Complex **1.**CH_3 crystallized in the same space group as **1.**Cl,[4] and the two structures are isomorphous, having a crystallographic C_2 axis coincident with the Fe−X bond. This symmetry gives a rigorously planar geometry at the iron atom in each case. The Fe−N distances are slightly longer in **1.**CH_3 (1.973(1) Å vs 1.948(2) Å), decreasing the bite angle of the β-diketiminate ligand (94.85(8)° vs 96.35(1)°) relative to **1.**Cl. The Fe−C bond is notable because **1.**CH_3 is the first crystallographically characterized three-coordinate iron−alkyl complex.[13] This bond is extremely short (2.009(3) Å), as one would expect from the low coordination number. The strong Fe−C interaction foreshadows the especially large effect of this ligand on the EFG of **1.**CH_3 shown below.

3.2. Mössbauer Studies. Figure 2A shows a 4.2 K Mössbauer spectrum of a polycrystalline sample of **1.**CH_3 recorded in the absence of an applied magnetic field. The spectrum consists of a quadrupole doublet with ΔE_Q = 1.74 mm/s and δ = 0.48 mm/s. The quadrupole splitting was found to be temperature-dependent (at 200 K we observed ΔE_Q = 1.57 mm/s), suggesting the presence of a low-lying excited state with orbital composition different from that of the ground state. The spectra in Figures 3 and 4 were obtained in magnetic fields **B** up to 8.0 T applied parallel to the observed γ-radiation. It can be seen that the applied field induces magnetic hyperfine interactions of considerable magnitude. To our knowledge, the internal field,

(11) Blessing, R. H. *Acta Crystallogr. A* **1995**, *51*, 33.
(12) *SHELXTL: Structure Analysis Program, version 5.04*; Siemens Industrial Automation Inc.: Madison, WI, 1995.
(13) Cambridge Structural Database (October, 2000). Allen, R. H.; Kennard, O. *Chem. Des. Autom. News* **1993**, *8*, 31−37.

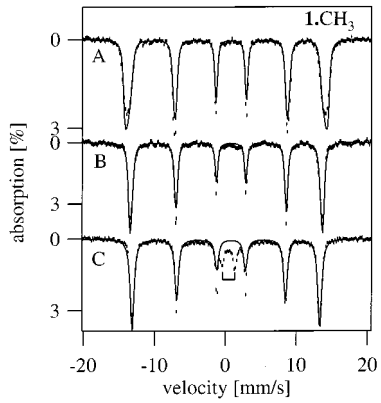

Figure 3. Mössbauer spectra of polycrystalline **1**.CH_3 recorded at 4.2 K in parallel applied fields of 8.0 T (A), 3.0 T (B), and 0.5 T (C). The magnetic splitting of the 0.5 T spectrum reflects an internal field of +82 T. The solid lines are spectral simulations based on eq 1 using the parameters listed in Table 1. The $\Delta m = 0$ transitions (lines 2 and 5) of the experimental data have slightly larger intensities than anticipated for a sample containing randomly oriented molecules, suggesting texture. See text for the doublet in (C) marked by the bracket. The simulations yield too small amplitudes for the middle two lines of the six-line magnetic spectrum, especially in (C). This mismatch is caused by the fact that B_{int} is somewhat distributed yielding a broadening that is larger for the outer lines; the simulation program uses a velocity-independent linewidth, which is too large for the inner two lines.

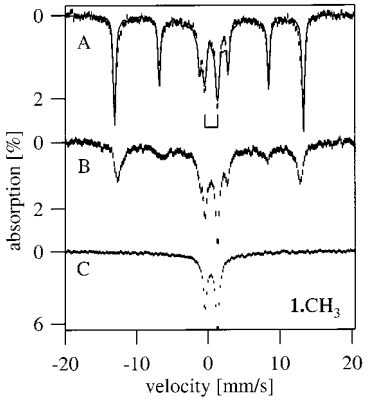

Figure 4. 4.2 K Mössbauer spectra of **1**.CH_3 recorded in parallel applied fields of 0.25 T (A), 0.15 T (B), and 0.05 T (C). The solid line in Figure 4A is a spectral simulation based on eq 1 using the parameters of Table 1 and assuming isotropic exchange coupling between two ferrous sites (J = 0.01 cm^{-1}). See text for the doublet in (A) marked by the bracket.

$\mathbf{B}_{int}$ = 82.0 T, observed for **1.**CH_3 exceeds those reported for other compounds by a considerable margin.[7] The maximum $\mathbf{B}_{int}$ is already observed in applied fields below 0.5 T. With increasing applied field, the effective field at the nucleus, $\mathbf{B}_{eff} = \mathbf{B}_{int} + \mathbf{B}$, also increases, showing that $\mathbf{B}_{int}$ is positive for the ground level. The observation of a large and positive $\mathbf{B}_{int}$ indicates that orbital contributions to the magnetic hyperfine field dominate. Given the large magnitude of the orbital contribution, it is anticipated that **1.**CH_3 has a very unusual electronic structure.

In general, high-spin Fe^{II} complexes are readily identified by their characteristic isomer shifts. However, three-coordinate iron complexes are rare, and thus an appropriate isomer shift database is not available. The X-ray structures of **1.**CH_3 and **1.**Cl show that the iron sites are formally Fe^{II}.[4] Because three ligands will produce a weak ligand field, a high-spin ($S = 2$) configuration is anticipated. In the following we will develop arguments that support such an assignment.

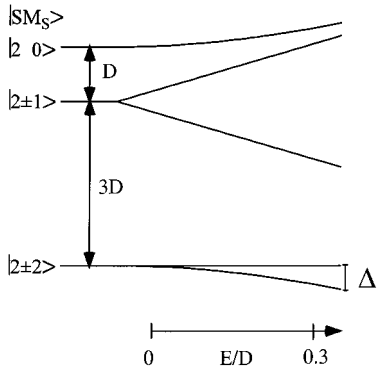

Figure 5. Energy level diagram for an $S = 2$ system for a large negative D as a function of the rhombicity E/D. The diagram is not strictly pertinent to the systems discussed but serves well for illustrating the principal features of the Mössbauer and EPR spectra.

For **1.**CH_3, a quadrupole doublet is observed in zero field, and magnetic hyperfine interactions arise only after an external magnetic field is applied. Such spectral behavior is characteristic of an integer spin paramagnet.[14] As can be seen from inspection of Figure 3, a fraction of molecules already exhibits fully developed magnetic splittings in applied fields of moderate strength, indicating an electronic system with a quasi-degenerate ground doublet having a small energy splitting Δ.[15] The spectral simulations described below suggest $\Delta \approx 0.03$ cm^{-1}. The observation of sizable magnetic splittings at low applied field also demonstrates that the intradoublet relaxation rate is slow at 4.2 K.

High-spin ($S = 2$) ferrous compounds are generally well described by the spin Hamiltonian,[16]

$$\hat{H} = D\left\{\hat{S}_z^2 - 2 + \frac{E}{D}(\hat{S}_x^2 - \hat{S}_y^2)\right\} + \beta\hat{\mathbf{S}}\cdot\mathbf{g}\cdot\hat{\mathbf{B}} + \hat{\mathbf{S}}\cdot\mathbf{A}\cdot\hat{\mathbf{I}} - g_n\beta_n\hat{\mathbf{B}}\cdot\hat{\mathbf{I}} + \hat{H}_Q \quad (1a)$$

and

$$\hat{H}_Q = \frac{1}{12}eQV_{z'z'}[3\hat{I}_{z'}^2 - I(I+1) + \eta(\hat{I}_{x'}^2 - \hat{I}_{y'}^2)] \quad (1b)$$

In eq 1, all quantities have their conventional meanings. The quadrupole interaction is expressed in the principal axes system (x',y',z') of the EFG tensor, where $V_{z'z'}$ is the largest component and $0 \le \eta \le 1/3$. For $|D| \gg \beta B$ and $D < 0$, the spin Hamiltonian has a ground doublet (see Figure 5) split by $\Delta = 3D(E/D)^2$. The parameters D and E/D can be used to produce a ground doublet with the desired Δ value that is well isolated from the excited sublevels of the $S = 2$ manifold. The ground doublet has a magnetization axis (z) along which the expectation values of the electronic spin saturate to $\langle S_z\rangle \approx \pm 2$ in fields above 0.1 T, while the components perpendicular to z, $\langle S_x\rangle$ and $\langle S_y\rangle$, remain near zero (see, for instance, ref 14). This behavior gives rise to

(14) (a) Münck, E. *Methods Enzymol.* **1978**, *54*, 346−379. (b) Münck, E. *Physical Methods in Inorganic and Bioinorganic Chemistry*; University Science Books: Sausolito, CA, 2000; Chapter 6, pp 287−319. (c) Münck, E. *The Porphyrins*; Academic Press: New York, 1979; Vol. IV, Chapter 8.

(15) Surerus, K. K.; Hendrich, M. P.; Christie, P.; Rottgardt, D.; Orme-Johnson, W. H.; Münck, E. *J. Am. Chem. Soc.* **1992**, *114*, 8579−8590.

(16) (a) Greenwood, N. N.; Gibb, T. C. *Mössbauer Spectroscopy*; Chapman and Hall: London, 1971. (b) Gütlich, P.; Link, R.; Trautwein, A. *Mössbauer Spectroscopy and Transition Metal Chemistry*; Springer-Verlag: Berlin, 1979. (c) Goldanski, V. I., Herber, R., Eds. *Chemical Applications of Mössbauer Spectroscopy*; Academic Press: New York, 1968.

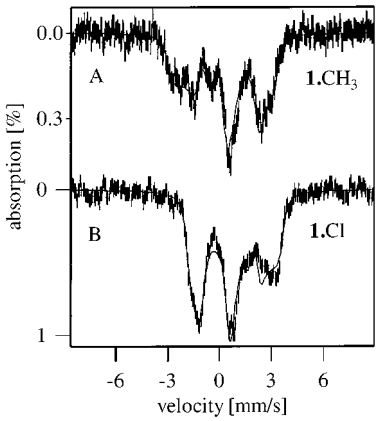

Figure 6. Mössbauer spectra of complex **1**.CH_3 (A) and **1**.Cl (B) recorded at 200 K in an 8.0 T applied field. The solid lines are theoretical curves based on eq 1 for the parameters listed in Table 1 assuming fast relaxation of the electronic spin. To separate the quasi-degenerate ground doublet from excited states we have used $D = -100$ cm^{-1}.

a uniaxial internal magnetic field $\mathbf{B}_{int} = -\langle \mathbf{S} \rangle \cdot \mathbf{A}/g_n\beta_n$.[14] Although the application of eq 1 to the complexes **1.**X is not strictly justified from a theoretical perspective (see section 4.1), we can use its features to simulate the Mössbauer spectra of the ground doublet. (In effect we are using eq 1 to emulate a fictitious $S = {}^1/_2$ spin Hamiltonian with $g_x = g_y = 0$ and an off-diagonal element $\Delta/2$). The *z*-component of the orbital contribution to the *A*-tensor for a high-spin ferrous ion with an isolated orbital ground state is given by $A_z(\text{orb}) = (g_z - 2)P$, where P is a scaling factor ($P \approx 40-60$ T) that depends on the radial extension of the 3d-orbitals, and g_z is the *z*-component of the *g*-tensor.[17] The saturation field for **1.**CH_3 which is attained when the $M_S = -2$ level is exclusively populated, $\mathbf{B}_{sat} = 2(g_z - 2)P \approx 82$ T, suggests $g_z \approx 2.8$, a value well in excess of the spin-only value, 2.

The solid lines drawn through the spectra of Figure 3 are spectral simulations based on eq 1 for $S = 2$, $D = -100$ cm^{-1}, and $E/D = 0.01$. This choice of parameters produces an isolated ground doublet with $\Delta = 0.03$ cm^{-1}. The 0.5 T spectrum of Figure 3 is characteristic of a uniaxial system, i.e., of a system for which $\mathbf{B}_{int}$ is directed along the electronic *z*-axis in essentially all molecules of the polycrystalline sample. $\mathbf{B}_{int}$ has Euler angles α_E and β_E relative to the principal axes system of the EFG tensor; β_E is the polar angle between *z* and *z*′, the latter being the principal axis belonging to the largest component of the EFG tensor. Quite frequently such situations lead to a manifold of equivalent solutions, referred to as the ambiguity problem.[8a] Our simulations, however, show that the largest component of the EFG tensor must be either perpendicular to the magnetization axis of the electronic system or tilted by 45° relative to this axis, i.e., $\beta_E = 90°$ or 45°. The molecular symmetry of the complex and the 200 K spectrum of Figure 6 (see below) do not support a solution for which $\beta_E = 45°$, so we are left with $\beta_E = 90°$. Since the component of the EFG tensor along $\mathbf{B}_{int}$ is negative, it follows that $\Delta E_Q > 0$. α_E is undetermined because the electronic ground doublet is uniaxial. We have arbitrarily chosen $\alpha_E = 0$, which directs $V_{z'z'}$ along *x*; this choice is supported by the molecular geometry (see section 4.1.1). The simulations shown in Figure 3 were obtained from eq 1 by using the parameters listed in Table 1. In the following we discuss some complications that render a precise analysis of the spectra quite difficult.

Table 1. Fine Structure and Hyperfine Parameters of **1.**X

ligand X	δ,[a] mm/s	ΔE_Q,[b] mm/s	η[b]	$\mathbf{B}_{int}$,[c] T	Δ,[d] cm^{-1}	g_{eff}[e]	μ_{eff}/β[f]
Cl^-	0.74	−1.61	0.5	+62	0.3	10.9(5)	5.4
$N'HTol^-$	0.71	+1.42	0.6	+78	$<10^{-3}$		5.3
$N'HtBu^-$	0.63	+1.11	0.2	+72	0.2		4.8
CH_3^-	0.48	+1.74	0.2	+82	0.03	11.4(1)	5.5

[a] Isomer shift relative to metallic iron at 298 K. [b] ΔE_Q and asymmetry parameter η are quoted in the x',y',z' system of eq 1b; $V_{z'z'}$, the largest component of EFG$^{(-)}$, is along the *x*-axis of the zero-field splitting tensor of eq 1a. See also footnote 21. [c] The internal magnetic field at ^{57}Fe nucleus is along the *z*-axis of the spin Hamiltonian eq 1a. For the crystal field analysis and the DFT calculations, the coordinate system in Figure 10 was used; in this system $\mathbf{B}_{int}$ is along the *x*-axis. [d] Zero-field splitting of $M_S = \pm 2$ states. [e] Effective g value for $M_S = \pm 2$ states obtained from EPR. [f] Effective magnetic moment at room temperature expressed in Bohr magnetons obtained from solution magnetic susceptibility measurements (precision $\pm 0.5\beta$).

Because the sample was suspended in Nujol to prevent orientation of the crystallites by the applied field, the spectra in Figure 3 were simulated with the assumption that the molecules are randomly distributed. This assumption, however, is not strictly justified. The spectra of Figures 3 and 4 exhibit texture effects that give rise to slightly increased intensities for the nuclear $\Delta m = 0$ transitions. This observation suggests that the crystallites have a tendency to settle in the Nujol host such that the magnetization axes of the molecules slightly favor a direction perpendicular to the γ beam. The presence of texture is also apparent in the spectrum of Figure 2A. Thus, least-squares fitting of the spectrum with two independent Lorentzian lines revealed that the area of the low-energy line is 2% larger than that of the high-energy line. The larger width of the low-energy line can be explained by noticing that the Earth's magnetic field (ca. 0.06 mT in Pittsburgh[18]) induces a hyperfine field of 0.8 T along the electronic *z*-axis in the presence of a dominant quadrupole interaction of positive sign along *x*.

Previous Mössbauer and EPR studies of integer spin paramagnets in our laboratory have revealed that Δ is generally distributed about some mean value.[15,19] Such distributions result in a broadening of integer-spin EPR signals (see section 3.3). The hyperfine field of molecules with larger Δ values saturates at higher fields than those of molecules with a smaller Δ. A distribution in Δ explains some of the spectral features in Figures 4B, such as the line broadening and the presence of a broad absorption feature that extends over the entire velocity range. However, the persistence of a doublet (7% of the total absorption) in fields as strong as 0.5 T requires amending the spin Hamiltonian with terms describing spin-dipolar and, perhaps, exchange interactions between neighboring complexes. The X-ray structure of **1.**CH_3 reveals pairs of molecules with Fe−Fe distances of 9.5 and 13 Å.[4] At these distances, neighboring molecules have dipolar coupling parameters of ca. 0.01

(17) Oosterhuis, W. T.; Lang, G. *Phys. Rev* **1969**, *178*, 439−456.

(18) Barton, C. E. *J. Geomagn. Geoelectr.* **1997**, *49*, 123−148.

(19) (a) Hendrich, M. P.; Münck, E.; Fox, B. G.; Lipscomb, J. D. *J. Am. Chem. Soc.* **1989**, *112*, 5861−5865. (b) Juarez-Garcia, C.; Hendrich, M. P.; Holman, T. R.; Que, L.; Münck, E. *J. Am. Chem. Soc.* **1991**, *114*, 518−525. (c) Fox, B. G.; Hendrich, M. P.; Surerus, K. K.; Andersson, K. K.; Froland, W. A.; Lipscomb, J. D.; Münck, E. J. *Am. Chem. Soc.* **1993**, *115*, 3688−3701. (d) Münck, E.; Surerus, K. K.; Hendrich, M. P. *Methods Enzymol.* **1993**, *227*, 463−479. (e) Yoo, S. J.; Angove, H. C.; Burgess, B. K.; Hendrich, M. P.; Münck, E. *J. Am. Chem. Soc.* **1999**, *121*, 2534−2545.

cm^{-1}.[20] Our Mössbauer simulation programs do not contain terms describing spin-dipolar interactions, but the effects of weak coupling are readily illustrated by assuming isotropic exchange coupling between two ferrous sites, $H_{exch} = J\mathbf{S}_1\cdot\mathbf{S}_2$. The spectral simulation shown in Figure 4A was obtained by using the parameters of Table 1 and $J = 0.01$ cm^{-1}. It can be seen that the simulation produces the doublet feature (bracket) in the center of the spectrum; this feature is absent for $J = 0$. The reader may keep in mind that a system consisting of two interacting complexes has four closely spaced levels that are nearly equally populated at 4.2 K; the doublet results from insufficiently decoupled spins, essentially the up/down and down/up combinations of an interacting pair. Texture, distribution of Δ, and dipolar couplings all affect the low-field spectra, and for these reasons precise simulations of these spectra are very difficult to achieve.

Because of the magnetic anisotropy of the electronic ground doublet, only the *z*-component of the magnetic hyperfine field can determined from the low-temperature spectra. Even for an 8.0 T applied field, the spectra do not indicate any Zeeman mixing between the ground doublet and excited states. For most high-spin ferrous compounds, the electronic spin relaxes rapidly above 100 K, so the internal magnetic field is proportional to the thermal expectation value $\langle\mathbf{S}\rangle_{th}$, $\mathbf{B}_{int} = -\langle\mathbf{S}\rangle_{th}\cdot\mathbf{A}/g_n\beta_n$.[14] Since the D values are generally smaller than 10 cm^{-1}, $\langle\mathbf{S}\rangle_{th}$ is essentially independent of D at 200 K. Under these circumstances, the *x*- and *y*-components of the magnetic hyperfine tensor can be determined as well. Figure 6A shows a Mössbauer spectrum of **1.**CH_3 recorded at 200 K in a parallel field of 8.0 T. This spectrum was simulated in the limit of fast fluctuations of the electronic spin, using the Hamiltonian of eq 1 and the parameters determined from the 4.2 K spectra. The simulations readily established that the 200 K spectrum reflects essentially the spectral features of the quasi-degenerate ground doublet, with only minor contributions of higher lying states. In the language of eq 1, the next group of electronic states has to be higher than 150 cm^{-1} ($|D| > 50$ cm^{-1}) to provide the correct magnetic splittings (see section 4.1). Smaller values of D would result in a significant population of the $M_S = \pm1$ levels resulting in reduced $\langle S_z\rangle_{th}$ values. Since $\langle S_x\rangle_{th} = \langle S_y\rangle_{th} = 0$ for the ground doublet, our data cannot provide estimates for the *x*- and *y*-components of the magnetic hyperfine tensor.

Interestingly, simulations with D values larger than 150 cm^{-1} produce $\langle S_z\rangle_{th}$ values at 200 K that are slightly too large, suggesting some population of excited states. This observation is in agreement with the zero-field spectra which show that ΔE_Q has declined by 10% relative to its value at 4.2 K. Our simulations of the 200 K spectrum rule out the possibility that the EFG is tilted by $\beta_E = 45°$ relative to the *z*-axis of the electronic system. Finally, the recoilless fraction at 200 K has declined by 80% relative to its value at 4.2 K, resulting in a high noise level at this temperature, despite accumulating 10^7 counts per velocity channel.

Although the spin Hamiltonian of eq 1 provides an adequate framework for simulating the spectra of complex **1.**CH_3, we do not wish to suggest that it properly describes the entire spin quintet. It describes well the low-temperature spectra and provides a large value of D, on the basis of which the zero-field splitting between the ground doublet and the next group of excited states is estimated to be ca. 150 cm^{-1}.[21]

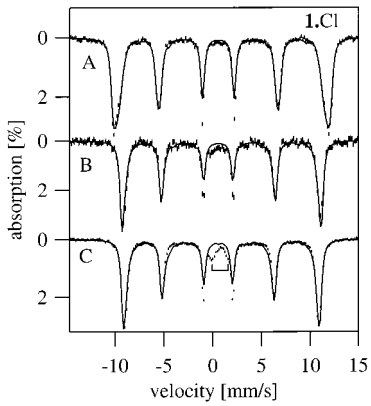

Figure 7. Mössbauer spectra of polycrystalline **1**.Cl recorded at 4.2 K in parallel applied fields of 8.0 T (A), 2.0 T (B), and 1.0 T (C). The magnetic splitting of the 1.0 T spectrum reflects an internal field of +62 T. See text for comments on the doublet in (C) marked by the bracket.

Figures 2B and 7 show 4.2 K spectra of polycrystalline **1.**Cl. The spectra of **1.**Cl have many similarities with those of **1.**CH_3, with some notable exceptions. The zero-field spectrum in Figure 2B consists of a quadrupole doublet with $\Delta E_Q = -1.61$ mm/s and $\delta = 0.74$ mm/s ($\Delta E_Q = -1.32$ mm/s at 200 K). As described for **1.**CH_3 the electronic ground state of **1.**Cl comprises a quasi-degenerate doublet that is well isolated from the excited states of the $S = 2$ manifold, and consequently the applied field spectra of **1.**Cl (Figure 7) have the same general features as those of **1.**CH_3. Again, the internal magnetic field is positive, but its magnitude, $\mathbf{B}_{int} = 62.0$ T, is smaller than the value $\mathbf{B}_{int} = 82.0$ T observed for **1.**CH_3. The best simulations to the field dependence of the spectra were obtained for $\Delta = 0.35$ cm^{-1}. As for **1.**CH_3, the largest component of the EFG tensor was found to be perpendicular to the direction of $\mathbf{B}_{int}$. Significantly, however, ΔE_Q of **1.**Cl is negative, suggesting that the two complexes have different orbital ground states (see, however, section 4.1.3). These conclusions are supported by the satisfying spectral simulation of the 200 K spectrum shown in Figure 6B.

In contrast to the sample of **1.**CH_3, polycrystalline **1.**Cl did not exhibit texture effects. This is most readily confirmed by noting that the two lines of the zero-field spectrum in Figure 2B have equal areas within the uncertainties of the fits. Note also that the low-energy line is not broadened as observed for **1.**CH_3. The lack of broadening reflects the fact that **1.**Cl has a significantly larger Δ value. From the parameters quoted in Table 1, a $\mathbf{B}_{int} = 60$ mT is predicted for $\mathbf{B}$(Earth) = 0.06 mT.[18]

3.3. EPR Studies. Figure 8, parts A and B, shows parallel-mode X-band EPR spectra of polycrystalline **1.**CH_3 and **1.**Cl recorded at 2 K. Both low-temperature spectra exhibit a broad asymmetric EPR transition with maxima at 59.4 and 35.6 mT for **1.**CH_3 and **1.**Cl, respectively. These transitions are observed up to 50 K, exhibiting a temperature dependence of the integrated intensity according to the Curie law.[22] We assign these

(20) Carlin, R. L. *Magnetochemistry*; Springer-Verlag: Berlin, 1986.

(21) In eq 1 we have used the standard form of a spin Hamiltonian, and for the chosen values of D and E/D the internal magnetic field, $\mathbf{B}_{int}$, will be along the electronic *z*-axis. The theoretical analysis presented in section 4.1 shows that the internal field is along the Fe−X bond. For the sake of the crystal field analysis, we adopt in section 4.1 the commonly used coordinate system for which the *z*-axis is perpendicular to the plane defined by the two diketiminate nitrogens and ligand X.

(22) Wertz, E. W.; Bolton, J. R. *Electron Spin Resonance*; McGraw-Hill: New York, 1972.

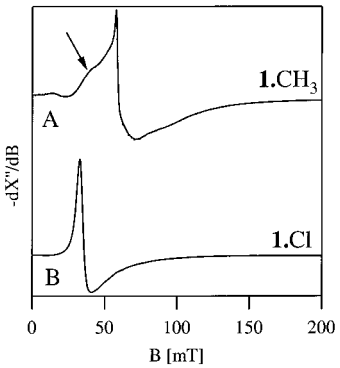

Figure 8. X-band EPR spectra of polycrystalline samples of **1**.CH_3 (A) and **1**.Cl (B) recorded in parallel mode at $T = 2.0$ K. The spectra were collected at a microwave frequency of 9.27 GHz, 20 μW microwave power, 0.98 mT modulation amplitude, and 100 kHz modulation frequency. The arrow in (A) denotes the shoulder discussed in the text.

resonances to a quasi-degenerate ($\Delta < 0.3$ cm^{-1}) $M_S = \pm 2$ ground doublet of an $S = 2$ multiplet. For this doublet, the resonance condition can be written as[15]

$$\Delta E = h\nu = \sqrt{\Delta^2 + (4g_z\beta B_z)^2} \qquad (2a)$$

For $\Delta \ll 4g_z\beta B_z$, as observed for **1.**CH_3, this expression can be expanded as

$$\Delta E \cong 4g_z\beta B_z + \frac{\Delta^2}{8g_z\beta B_z} = g_{\text{eff}}\beta B_z\left(1 + \frac{\Delta^2}{2(g_{\text{eff}}\beta B_z)^2}\right) \qquad (2b)$$

For **1.**CH_3, the second term in the parentheses of eq 2b will be about 0.01, and thus a value of $\Delta = 0.03$ cm^{-1} gives $g_{\text{eff}} = 11.4$. The spectrum of Figure 8A exhibits a shoulder at $g = 16.7$, which may reflect the presence of spin-dipolar interactions in the solid or, alternatively, may represent a distribution of Δ values. For small Δ values the intensity of the resonance is proportional to $\Delta^2/(g_{\text{eff}}\beta B_z)^2$.[15] Spectral simulations based on this expression suggest that the $g = 16.7$ shoulder represents less than 1% of the molecules. EPR spectra of frozen toluene solutions of **1.**CH_3 (not shown) lack this shoulder but still exhibit the sharp feature at $g_{\text{eff}} = 11.4$. Since the Mössbauer spectra of **1.**CH_3 are obtained for polycrystalline samples, we have displayed a representative EPR spectrum of a solid sample in Figure 8A. Taking into account the uncertainties in Δ, we estimate $g_{\text{eff}} = 11.30-11.46$, where the upper bound is the theoretical maximum for g_{eff} (see section 4.1.1).

The Mössbauer data for **1.**Cl suggest that $\Delta = 0.35$ cm^{-1}, and therefore the general expression (eq 2a) has to be used to describe the EPR resonance. Since the terms in eq 2a have comparable magnitudes, g_{eff} cannot be determined from a spectrum taken at a single frequency. However, given that g_{eff} is theoretically confined to $8.0 < g_{\text{eff}} < 11.46$, Δ can be constrained from the spectrum of Figure 8B to 0.255−0.284 cm^{-1}. We have also taken an X-band spectrum in perpendicular mode (not shown); in this mode the cavity is tuned at a slightly higher frequency, which allowed us to limit g_{eff} to the range 10.4−11.46.

4. Discussion

4.1. Crystal Field Model for 1.X. 4.1.1. Fine Structure and Orbital Angular Momentum in 1.X. The spectroscopic results for **1.**X (X = Cl^-, $NHTol^-$, $NHtBu^-$, CH_3^-) demonstrate that the iron sites are high-spin in these complexes. This spin state is suggested by the low coordination number for Fe and is further corroborated by the large effective g values and effective magnetic momenta (see Table 1).[23] The lowest two sublevels of the spin quintet are combinations of $M_S = \pm 2$ states that are closely spaced in energy (see Table 1) and separated from the next sublevels of the same spin manifold by at least 150 cm^{-1}. The spin quantization axis, denoted ξ and defined by $S_\xi|\pm 2\rangle = \pm 2|\pm 2\rangle$, was found to be perpendicular to the principal axis of the EFG tensor, that corresponds to the eigenvalue with the largest magnitude. (N.B.: Direction ξ corresponds to the z-direction in the spin Hamiltonian (eq 1a), written in a "proper" coordinate frame for which $0 \le E/D \le {}^1/_3$.) $\mathbf{B}_{\text{int}}$ is positive along ξ, in contrast to the internal fields in virtually all high-spin ferrous complexes. This observation, the large zero-field splittings of the $S = 2$ multiplet, and the g_{eff} and μ_{eff} values in excess of the spin-only values $g_{\text{eff}} = 8$ and $\mu_{\text{eff}} = 4.9\ \beta$ suggest the presence of substantial unquenched orbital momenta. $\mathbf{B}_{\text{int}}$ contains three contributions, viz. the Fermi contact term, arising from spin polarization of the s electrons by exchange interactions with the unpaired 3d electrons, an orbital term representing the magnetic field induced by the orbital motion of the 3d electrons, and the spin dipolar term associated with a nonspherical spin density in the 3d shell:[16]

$$\mathbf{B}_{\text{int}} = \mathbf{B}_{\text{fc}} + \mathbf{B}_{\text{L}} + \mathbf{B}_{\text{dp}} = 2\beta\langle r^{-3}\rangle(\kappa\langle\hat{\mathbf{S}}\rangle - \langle\hat{\mathbf{L}}\rangle) + \mathbf{B}_{\text{dp}} \quad (3)$$

where κ is a dimensionless constant expressing the s-orbital contribution. Orbital angular momentum in common high-spin ferrous complexes is almost quenched under the influence of the crystal field.[24] Some orbital momentum usually persists as a result of crystal field state mixing by spin−orbit coupling. The size of the resulting orbital momentum is then approximately proportional to the ratio of the spin−orbit coupling constant λ and the crystal field splitting $\Delta\epsilon_{\text{crys}}$. As the crystal field splittings are typically an order of magnitude larger than λ, the resulting orbital terms are small. The idealized C_{2v} symmetry of **1.**X gives rise to crystal field states which transform according to one-dimensional irreducible representations. These states have quenched orbital angular momenta. However, the momenta observed in **1.**X are large and suggest that there is a substantial state mixing by spin−orbit coupling. For this "unquenching" mechanism to be effective, the orbital ground state must be accidentally degenerate, or nearly so, with a low-lying excited orbital level. All pairs of 3d-orbitals whose energy separations could possibly be small have been listed in Table 2. For $g_{\text{eff}}\beta B \ge k_B T$, the expectation values in eq 3 can be evaluated for the lowest level of the Zeeman-split spin quintet. In the absence of an applied magnetic field, the internal field is quenched by the zero-field splitting Δ (both $-\langle S_\xi\rangle$ and $-\langle L_\xi\rangle$).

(23) The experimental effective magnetic moments at room temperature for **1.**CH_3 and **1.**Cl are clearly above the spin-only value of 4.9 μ_B ($S = 2$). Our crystal field model predicts for **1.**CH_3 and **1.**Cl powder-averaged magnetic moments of 5.47 and 5.38 μ_B at 300 K, respectively. We have performed SQUID susceptibility studies on polycrystalline samples between 4 and 300 K, but we encountered problems in reproducing the temperature dependence of the effective magnetic moments, which might be attributable to alignment of the crystallites by the applied magnetic field. Such alignment is not surprising in view of the extreme magnetic anisotropy of the ground doublet. For the Mössbauer studies we have supressed alignment by suspending the polycrystalline samples in Nujol. Further SQUID susceptibility studies are in preparation.

(24) Pavel, E. G.; Kitajima, N.; Solomon, E. I. *J. Am. Chem. Soc.* **1998**, *120*, 3949−3962.

Table 2. Effective *g* Values, Angular Momenta, and Spin Quantization Axes of High-Spin Ferrous Ion with a Doubly Degenerate Orbital Ground State

degenerate orbitals[a]	g_{eff}	α[b]	spin quant. axis[c]
z^2 x^2-y^2	8	0	
z^2 xy	8	0	
xz xy	10	1	x
yz x^2-y^2	10	1	x
yz xy	10	1	y
xz x^2-y^2	10	1	y
xz yz	10	1	z
yz z^2	11.5	$\sqrt{3}$	x
xz z^2	11.5	$\sqrt{3}$	y
xy x^2-y^2	12	2	z

[a] Orbitals labeled d and d′ in Supporting Information (eqs S.1). z^2 stands for $3z^2-r^2$. [b] Expectation value $-\langle L_\xi\rangle$ in lowest magnetic sublevel. [c] Denoted ξ in eq 4.

However, since Δ is small (Table 1), a large $\mathbf{B}_{int}$ can easily be generated by applying a magnetic field with a nonvanishing component along the spin quantization axis. The values for $-\langle L_\xi\rangle$ to be used in eq 3 are listed in Table 2. These values are the maximum orbital momenta attainable for the orbital pairs and pertain to the limit in which the crystal field splitting between these orbitals vanishes. If the smallest term in eq 3, $\mathbf{B}_{dp}$, is ignored, $-\langle L_\xi\rangle$ can be expressed as

$$-\langle \hat{L}_\xi\rangle = 2\kappa\frac{B_{fc,\xi} - B_{int,\xi}}{B_{fc,\xi}} \qquad (4)$$

The values for $-\langle L_\xi\rangle$ in Table 2 can be compared with the experimental values obtained from eq 4 by substituting $\mathbf{B}_{int} \approx$ 70 T (Table 1), $\mathbf{B}_{fc} \approx -50$ T (based on the estimate of 12.7 T per unpaired electron; see ref 16a), and $0.2 < \kappa < 0.4$ into this expression. The substitution yields $0.96 < -\langle L_\xi\rangle < 1.92$, which includes seven of the cases listed in Table 2.

Fortunately, g_{eff} provides a more discriminatory criterion for selecting the lowest orbital pair. The effective *g* value arising from spin−orbit coupling between crystal field split 3d-orbitals d and d′ is given by

$$g_{eff} = 2g_eS + 2\alpha\cos[2\Theta] \qquad (5a)$$

where Θ describes mixing of the two states under the influence of crystal field and spin−orbit coupling,

$$\Theta = \arctan\left(\left|\frac{4\lambda\alpha}{\epsilon_d - \epsilon_{d'}}\right| - \sqrt{\left(\frac{4\lambda\alpha}{\epsilon_d - \epsilon_{d'}}\right)^2 + 1}\right) \qquad (5b)$$

$\lambda = -107$ cm^{-1} is the spin−orbit coupling constant[25] in $\lambda\hat{\mathbf{L}}\cdot\hat{\mathbf{S}}$, $S = 2$, $g_e = 2.0023$, $\epsilon_d - \epsilon_{d'}$ is the crystal field splitting, and α is a coefficient of which the value is listed in Table 2 for each orbital pair. In the limits of small and large crystal field splittings, eq 5a simplifies to:

$$g_{eff} \approx 8 + 2\alpha - \frac{1}{\alpha}\left(\frac{\epsilon_d - \epsilon_{d'}}{4\lambda}\right)^2, \quad \left|\frac{\epsilon_d - \epsilon_{d'}}{\lambda}\right| \ll 1 \qquad (5c)$$

$$g_{eff} \approx 8 + 8\alpha^2\left|\frac{\lambda}{\epsilon_d - \epsilon_{d'}}\right|, \quad \left|\frac{\lambda}{\epsilon_d - \epsilon_{d'}}\right| \ll 1 \qquad (5d)$$

Figure 9 shows the g_{eff} values as a function of $(\epsilon_d - \epsilon_{d'})/\lambda$. It can be seen that g_{eff} depends on the magnitude of $\epsilon_d - \epsilon_{d'}$ but not on its sign. The maximum of g_{eff} is obtained at $\epsilon_d = \epsilon_{d'}$ for each orbital pair. These maxima, which can be evaluated by substituting $\epsilon_d - \epsilon_{d'} = 0$ in eq 5c, are listed in the second column of Table 2. The experimental g_{eff} values can be compared with the predicted maxima. The first seven cases yield maxima for g_{eff} that are lower than the g_{eff} values observed in the series **1.**X and can therefore be excluded. Two of the remaining three cases, listed in the last lines of the table, can be eliminated, based on the following qualitative crystal field considerations.

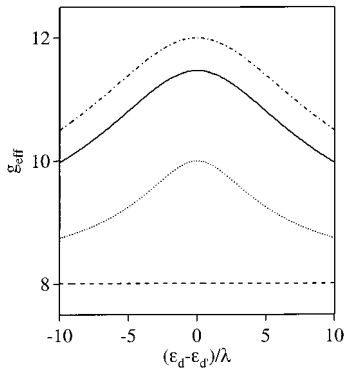

Figure 9. Plot of g_{eff} values as a function of $(\epsilon_d - \epsilon_{d'})/\lambda$ for $\alpha = 0$ (dashed line), 1 (dotted line), $\sqrt{3}$ (full line), and 2 (dash-dotted line) in eq 5a.

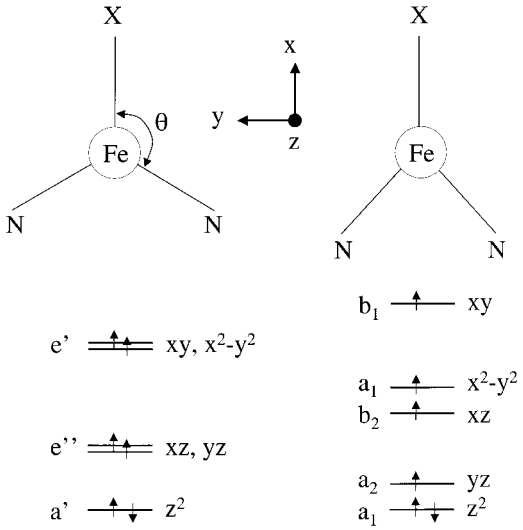

Figure 10. Central structural core in complexes **1**.X with an idealized trigonal geometry (left) and a realistic distorted geometry (right) together with schematic 3d-orbital level schemes. The *z*-axis of the Cartesian coordinate frame is parallel to the trigonal axis and points toward the reader. The symmetry labels refer to C_{3h} (left) and C_{2v} symmetry and ignore the differences between the ligands.

Figure 10 shows the core of **1.**X with idealized planar trigonal symmetry ($\theta = 120°$) and a schematic representation of the actual distorted geometry of these complexes ($\theta \approx 132°$). Also shown are the corresponding qualitative orbital schemes which illustrate the removal of the degeneracies from the e-symmetry orbitals by the crystal field in the distorted structure.[26] The *xy* orbital is raised in energy relative to x^2-y^2 because the diketiminate nitrogens form nearly a 90° angle at the iron, which places them favorably in the lobes of the *xy* orbital. In the unlikely case that the splitting between *xy* and x^2-y^2 were large enough to stabilize x^2-y^2 as the ground state, the large splitting

(25) Bendix, J.; Broson M.; Schäffer, C. E. *Inorg Chem.* **1993**, *32*, 2838−2849.

(26) Campanion, A. L.; Komarynsky, M. A. *J. Chem. Educ.* **1964**, *41*, 257−262.

($>10^4$ cm^{-1}) would essentially quench the orbital momentum arising from this orbital pair. Hence, the last case in Table 2 can be excluded as well. To decide between the remaining two cases, (yz, z^2) and (xz, z^2), we note that yz is located in a plane perpendicular to the Fe−X vector, whereas xz is in the plane bisecting the N−N vector. Increasing θ increases (decreases) the spatial overlap between xz (yz) and the symmetric (antisymmetric) combination of the nitrogen p_z-orbitals, splitting xz and yz as indicated in Figure 10. Thus, we conclude that the large orbital momenta in **1.**X originate from spin−orbit coupling between the z^2 and yz levels. Substitution of the maximum of $-\langle L_\xi \rangle$ for the (yz, z^2) pair into eq 3 yields $\kappa \approx 0.33$, which is in the middle of the range reported for this quantity.[17]

The last column in Table 2 indicates the quantization axis (ξ) of the spin, using the Cartesian coordinates defined in Figure 10 as a reference frame. Thus, the present analysis specifies the spatial relationship between the principal axes of the fine-structure and hyperfine tensors in the spin Hamiltonian with respect to the molecular frame. For each orbital pair in Table 2, there is only one Cartesian component of the orbital angular momentum operator that yields a nonzero matrix element, e.g., $\langle z^2|L_x|yz\rangle = i\sqrt{3}$. Thus, the spin−orbit coupling operator in the space spanned by basis $\{z^2, yz\}$ simplifies to

$$\lambda \hat{\mathbf{L}}\cdot\hat{\mathbf{S}} \rightarrow \lambda \hat{L}_x \hat{S}_x \tag{6}$$

For $\epsilon_{yz} = \epsilon_{z^2}$, the Hamiltonian can be diagonalized by using the orbital states,

$$|\Psi_\pm\rangle = (|z^2\rangle \pm i|yz\rangle)/\sqrt{2} \tag{7}$$

and spin states that are quantized along x, i.e., $S_x|M_S\rangle = M_S|M_S\rangle$. The energy eigenvalues can now be expressed as

$$\epsilon_{M_S} = -|\lambda|\langle\Psi_\pm|\hat{L}_x|\Psi_\pm\rangle\langle M_S|\hat{S}_x|M_S\rangle \tag{8a}$$

in which the matrix elements are given by

$$\langle\Psi_\pm|\hat{L}_x|\Psi_\pm\rangle = \mp\sqrt{3} \tag{8b}$$

$$\langle M_S|\hat{S}_x|M_S\rangle = M_S \tag{8c}$$

The states, $|\Psi_\pm, M_S\rangle = A|\Psi_\pm\rangle|M_S\rangle$ (A is an antisymmetrizer), and energies arising from spin−orbit coupling between the two degenerate crystal field levels are given by

$$\begin{aligned}
&|\Psi_+,2\rangle, |\Psi_-,-2\rangle, \quad \epsilon_{\pm 2}{}^{+} = 2\sqrt{3}|\lambda| \\
&|\Psi_+,1\rangle, |\Psi_-,-1\rangle, \quad \epsilon_{\pm 1}{}^{+} = \sqrt{3}|\lambda| \\
&|z^2,0\rangle, |yz,0\rangle, \quad \epsilon_0 = 0 \\
&|\Psi_-,1\rangle, |\Psi_+,-1\rangle, \quad \epsilon_{\pm 1}{}^{-} = -\sqrt{3}|\lambda| \\
&|\Psi_-,2\rangle, |\Psi_+,-2\rangle, \quad \epsilon_{\pm 2}{}^{-} = -2\sqrt{3}|\lambda|
\end{aligned} \tag{9}$$

The energies in eq 9 depend linearly on the coupling constant λ, and accordingly, the level energies increase linearly with the magnetic quantum number. Spin−orbit coupling between nondegenerate orbital levels, such as those between the designated orbital pair and the remaining three d-orbital states in **1.**X, give rise to a scheme with splittings depending quadratically on λ in which the term energies progress as a quadratic function of the magnetic quantum number. The latter type of interaction is commonly parametrized by the DS_ξ^2 term in the spin Hamiltonian formalism.[27] However, as the second-order perturbation terms are typically smaller by a factor $\lambda/\Delta\epsilon_{crys}$ than the first-order terms, the energies and states given in eq 9 should provide good approximations to those obtained from a complete treatment. The inability of the DS_ξ^2 operator to represent the entire energy spectrum of the spin quintet does not invalidate the spectroscopic data analysis based on the quadratic spin Hamiltonian eq 1a, because a precise description of the level spacings is irrelevant at the employed cryogenic temperatures, where the excited zero-field levels are virtually depopulated. The zero-field splitting attains the maximum value $|\lambda|\sqrt{3} = 120-170$ cm^{-1} in the degenerate case.

The smallness of the crystal field splitting between the z^2 and yz orbitals introduces the concern of state mixing by low-symmetry components of the crystal field,

$$\begin{aligned}
|d\rangle &= \cos\vartheta|z^2\rangle + \sin\vartheta|yz\rangle \\
|d'\rangle &= -\sin\vartheta|z^2\rangle + \cos\vartheta|yz\rangle
\end{aligned} \tag{10a}$$

where, contrary to the case of spin−orbit mixing, the coefficients are real numbers. The only nonzero matrix element of the angular momentum operator in the representation $\{d,d'\}$ is an invariant of the transformation 10a,

$$\langle d|L_x|d'\rangle = \langle z^2|L_x|yz\rangle \tag{10b}$$

and, therefore, the effective g value is not affected by any such crystal field effect.

The magnitude of the crystal field splitting $|\epsilon_{yz} - \epsilon_{z^2}|$ between the lowest two 3d-orbitals in **1.**X can be evaluated from eq 5a, using the value for g_{eff} and an estimate for λ. The evaluation results in the splittings 452 cm^{-1} for **1.**Cl and 135 cm^{-1} for **1.**CH_3, where we have adopted the g_{eff} values listed in Table 1 and the rounded free ion value $\lambda = -100$ cm^{-1}. (N.B.: Equation 5c gives 395 and 133 cm^{-1}, respectively, and illustrates its accuracy, particularly in the second case.) Thus, the crystal field splitting in **1.**Cl is larger than that in **1.**CH_3, quenching the orbital angular momentum to a greater extent than in **1.**CH_3, and reducing the net internal field (eq 3) by an amount close to that observed (Table 1). The last statement follows from the expression for the change in the magnetic hyperfine orbital term, $\Delta A_L = {}^1/_2\, B_L(CH_3)[g_{eff}(CH_3) - g_{eff}(Cl)]/[g_{eff}(CH_3) - 8]$, from which we predict a difference of 20−40 T in $\mathbf{B}_{int}$ for the two complexes. However, to determine whether z^2 or yz is the ground state, we have to resort to an analysis that includes zero-field splitting Δ and the EFG tensor.

4.1.2. Evaluation of the Zero-Field Splitting Δ. The $M_S = \pm 2$ ground state of the truncated spin−orbit coupling operator that exclusively acts between the z^2 and yz states in the $3d^6$ $S = 2$ manifold is strictly degenerate (see eqs 6−9). The actual levels, however, were found to be split by energy Δ in zero applied field (see Table 1). These splittings originate from spin−orbit couplings between the sets $\{z^2,yz\}$ and $\{xz,xy,x^2-y^2\}$, which generate orbital angular momenta perpendicular to the spin quantization axis, x. It follows from Table 2 that the

(27) (a) Abragam, A.; Bleaney, B. *Electron Paramagnetic Resonance of Transition Ions*; Clarendon Press: Oxford, 1970. (b) Griffith, J. S. *The Theory of Transition-Metal Ions*; Cambridge University Press: Cambridge, 1971.

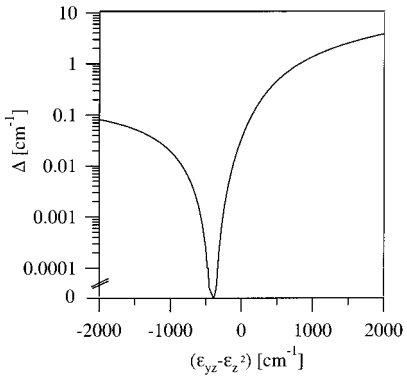

Figure 11. Δ calculated as a function of crystal-field splitting ($\epsilon_{yz} - \epsilon_{z^2}$) for $\epsilon_{xz} = 3500$ cm^{-1}. The ordinate is on a logarithmic scale with an axis break between 0 and 0.0001.

interactions in the pairs (z^2,*xz*), (*yz*,*xz*), and (*yz*,*xy*) have the required property. Among these interactions, the one involving *xy* is expected to have the least effect on Δ, because *xy* is the highest 3d-orbital level with an estimated excitation energy of ~12 000 cm^{-1} (see section 4.2). The zero-field splitting Δ was calculated by numerical diagonalization of

$$\mathscr{H} = \mathscr{H}_{CF} + \lambda \hat{\mathbf{L}} \cdot \hat{\mathbf{S}} \tag{11a}$$

where the first term represents the crystal field which splits the 3d-obital energies into a pattern such as the one shown in Figure 10 on the right. The calculation gives the eigenstates

$$|\Psi_n\rangle = \sum_{M_S,M_L} c^{(n)}_{M_S,M_L} |M_S,M_L\rangle \tag{11b}$$

and energy eigenvalues, ϵ_n, from which Δ is evaluated by taking the difference of the lowest two values, $\epsilon_1 - \epsilon_0$. These calculations were performed for different sets of orbital energies and revealed a large effect of the order of the crystal field energies for z^2 and *yz* on Δ. The behavior can be understood by considering the approximate expression

$$\Delta \approx \sqrt{3}\left(\frac{\sqrt{3}-1}{\sqrt{2}}\right)^2 \frac{|\lambda|^3}{(\epsilon_{xz} + \sqrt{3}|\lambda|)^2} \tag{11c}$$

which was derived by a perturbational treatment of the effect of spin−orbit coupling involving the $|xz,M_S\rangle$ states with crystal field excitation energy ϵ_{xz} on the energies of the degenerate $M_S = \pm 2$ ground levels for $\epsilon_{yz} = \epsilon_{z^2} = 0$, given in eq 9. The terms $\sqrt{3}$ and −1 in the quadratic factor in eq 11c originate from the couplings of *xz* with the z^2 and *yz* components of the orbital ground state given in eq 7, respectively. The two contributions have opposite signs and tend to cancel. In the presence of a crystal field splitting between z^2 and *yz*, among other things, the factor has to be replaced by the more general form $\sqrt{3}\sin\gamma - \cos\gamma$, where γ is defined as in eq S.1a of the Supporting Information. The weight of the negative cosine term increases if the *yz* orbital is lowered by the crystal field relative to z^2 in energy. As a result, Δ decreases until perfect cancellation is attained at $\gamma = {}^1/_6\,\pi$, for which $\Theta = \gamma - {}^1/_4\,\pi = -{}^1/_{12}\,\pi$. Substituting Θ into eq 5b and solving for the crystal field splitting yields the condition $\epsilon_{yz} - \epsilon_{z^2} = -4|\lambda|$ for $\Delta = 0$. The value of Δ increases again for $\epsilon_{yz} - \epsilon_{z^2} < -4|\lambda|$ but does not become anywhere as large as for $\epsilon_{yz} - \epsilon_{z^2} > 0$ (see Figure 11). Thus, unlike the effective *g* value, Δ is a nonsymmetric function of $\epsilon_{yz} - \epsilon_{z^2}$, having large and small values for positive and negative arguments, respectively, and is therefore a sensitive marker of the sign of the crystal field splitting. Based on the experimental value for Δ in **1.**Cl (Table 1), ϵ_{xz} is estimated to be 3600 cm^{-1} for $\epsilon_{yz} - \epsilon_{z^2} = 400$ cm^{-1} and 100 cm^{-1} for $\epsilon_{yz} - \epsilon_{z^2} = -400$ cm^{-1}. (N.B.: The magnitudes used here for the crystal field splittings were estimated from g_{eff} (see section 4.1.1); the energies of the remaining 3d-orbitals were obtained from the TD-DFT calculations described in section 4.2.2.) These estimates concern the denominator of eq 11c and reflect the change in the numerator associated with the sign flip of the crystal field splitting between z^2 and *yz* at fixed Δ. The corresponding values for **1.**CH_3 (i.e., $\epsilon_{xz} - \epsilon_{yz} = 6000$ and 1500 cm^{-1} for $\epsilon_{yz} - \epsilon_{z^2} \approx \pm 130$ cm^{-1}, respectively) show the same trend as that found in **1.**Cl but are overall larger because Δ for **1.**CH_3 is smaller than that in the chloride complex (see Table 1). The splitting $\epsilon_{xz} - \epsilon_{yz} \approx 100$ cm^{-1} obtained for **1.**Cl by assuming that *yz* is the ground state of the crystal field seems to be unrealistically small for a metal ion in a severely distorted trigonal coordination sphere. Indeed, TD-DFT suggests that the energy separation for this orbital pair is at least 1 order of magnitude larger (section 4.2.2). The splitting $\epsilon_{xz} - \epsilon_{yz} \approx 3600$ cm^{-1} estimated in the presence of a z^2 ground state is on the right order of magnitude, and we therefore conclude that z^2 is the ground state of the crystal field in **1.**Cl.

Given that splitting $\epsilon_{yz} - \epsilon_{z^2}$ in **1.**CH_3 has a magnitude of only 135 cm^{-1}, a determination of its sign may seem to be a rather academic exercise. One could argue that by replacing a $\sigma-\pi$ donor (Cl^-) with a σ donor (CH_3^-), the energy gap $\epsilon_{xz} - \epsilon_{yz}$ (which depends on the π interaction of *xz* with X) will drop. This prediction seems to support a *yz* ground state in **1.**CH_3, because $\epsilon_{xz} - \epsilon_{yz} \approx 1500$ cm^{-1} obtained for **1.**CH_3 with a *yz* ground state is smaller than the value 3600 cm^{-1} for **1.**Cl. However, we consider the size of the reduction thus obtained (2100 cm^{-1}) to be unrealistically large. This judgment is based on TD-DFT calculations for **1.**Cl and **1.**CH_3 (section 4.2.2) that result in nearly equal $\epsilon_{xz} - \epsilon_{yz}$ values (≈4650 cm^{-1}) for the two species and indicate that the splitting between *xz* and *yz* is predominantly determined by the metal−diketiminate interactions. The alternative possibility of a z^2 ground state, for which $\epsilon_{xz} - \epsilon_{yz}$ (6000 cm^{-1}) is found to be greater than the value for **1.**Cl (3600 cm^{-1}), is not satisfactory either. It should be noted, however, that while these estimates are based on a common (free-ion) value for $|\lambda|$,[25] the value for $\epsilon_{xz} - \epsilon_{yz}$ obtained from eq 11c for a given value of Δ diminishes if one adopts a smaller value for $|\lambda|$. In particular, a lowering of $|\lambda|$ in **1.**CH_3 by 30% reduces $\epsilon_{xz} - \epsilon_{yz}$ from 6000 cm^{-1} to about 3600 cm^{-1}. Taking into consideration that a 30% reduction in $|\lambda|$ is not unprecedented and that the computational results presented in section 4.2 support a z^2 ground state, we tentatively conclude that z^2 is the ground state of the crystal field in **1.**CH_3. Finally, given that z^2 is lowest in **1.**Cl, the decrease of $\epsilon_{yz} - \epsilon_{z^2}$ in passing from **1.**Cl (435 cm^{-1}) to **1.**CH_3 (135 cm^{-1}) can be rationalized by noting that ϵ_{z^2} increases (due to an enhanced σ interaction between z^2 and X), while ϵ_{yz} is constant (due to a lack of σ and π interactions between *yz* and X).

In summary, the analysis of the Δ values supports the idea that the z^2 orbital is the lowest 3d level in the crystal field of the chloride complex, and most likely so in the methyl complex.

4.1.3. Evaluation of the Electric Field Gradient Tensor. The sign of the EFG[28] is determined by the electronic charge distribution about the Fe nucleus. In particular, an oblate charge distribution, such as that found for an electron in a *yz* orbital, gives rise to $\Delta E_Q > 0$, whereas a prolate distribution, as in the case of an occupied z^2 orbital, yields $\Delta E_Q < 0$.[16] Table 1 shows that ΔE_Q is negative in **1.**Cl and positive in **1.**CH_3, suggesting that the ground orbitals in these systems are z^2 and *yz*, respectively. However, this suggestion is incorrect because the V_{max} components[28] in the two complexes are perpendicular to the spin quantization axes (see section 3.2). The V_{max} values associated with electrons in the z^2 and *yz* orbitals are along the *z*- and *x*-axes, respectively. As the spin is predicted to be quantized along *x*, irrespective of the order of the two orbitals, we would indeed obtain the observed perpendicular orientation for a z^2 ground state but a parallel orientation (along *x*, i.e., the Fe−X vector) for a *yz* ground state. Thus, the observed sign flip in ΔE_Q cannot be attributed to a reversal in the order of the two orbitals and requires a more thorough analysis.

So far we have only considered the valence contributions to the EFG. To explain the rather volatile behavior of the EFG in the **1.**X series, we have extended our analysis by taking into consideration two additional contributions, namely: (i) the effect of spin−orbit coupling on the valence part of the electric field gradient and (ii) ligand contributions to the electric field gradient, arising from the unusual coordination geometry at the metal. The $S = 2$ state of **1.**X results from a half-filled shell with five spin-parallel (α) electrons, a sixth electron with minority spin (β) aligned antiparallel to the majority spin, and a large number of spin-paired electrons. The charge distribution in the molecule can be decomposed into a distribution for the sixth electron and one for the other electrons in the system. The two distributions yield EFG tensors at the iron nucleus which we generically refer to as the "metal contribution" and the "ligand contribution" to the EFG.[29] In general, the ligands influence the metal contribution by splitting the degenerate 3d manifold into a nondegenerate set of crystal field states and by admixing ligand orbitals into the 3d-orbitals by which they are delocalized toward the ligands. We show in section 4.2 by applying TD-DFT that the delocalization of the 3d-orbitals in **1.**X is much smaller than expected on the basis of molecular orbital calculations. This circumstance greatly facilitates the evaluation of the influence of the spin−orbit coupling between the ground state and the nearby excited states on the EFG by allowing a crystal field treatment. A detailed analysis of the metal contribution is presented in section S.1 of the Supporting Information. The ligand contributions to the EFG originate from the anisotropy in the charge distribution around the iron nucleus, arising from all charges in the complex other than the sixth 3d electron. The relevant charges are located in the essentially non-overlapping metal−ligand areas and furnish additive contributions to the EFG with respect to the ligands. These contributions are parametrized by the ligand-specific quantities W_X, where X refers to a ligand, which are assumed to be transferable between the complexes. Departures from transferability are expected when, upon replacing a ligand in the coordination shell of the three-coordinate iron site, the charge distributions in the two unaltered bonds are modified. However, the DFT calculations presented in section 4.2 indicate that these nonadditivity effects are small compared to the magnitude of the W_X parameters. The details of the analysis of the ligand contributions to the EFG in the series **1.**X are presented in section S.2 of the Supporting Information. The effects of spin−orbital coupling and covalent reduction on the metal contribution to the EFG have been parametrized by the admixing parameter υ and the reduction factor *f*, respectively, which are defined in section S.1. The values for υ and *f* can be confined to narrow ranges, based on the *g* values (Figure S.1, Supporting Information) and DFT calculations. These constraints have been combined with the electric hyperfine data to construct the allowed areas in a graphical representation of the W_X parameters (Figures S.2−4). The solutions lie in areas in which either *yz* or z^2 is the ground state. As the latter state is the ground state according to the analysis of Δ given in section 4.1.2, the domains where z^2 is lowest must contain the solution. The limiting values for the W_X parameters obtained from this analysis have been listed in the last column of Table 3. The values for W_X are comparable in magnitude to the metal contributions to the EFG. For example, a single methyl ligand may yield a quadrupole splitting of as much as −2 mm/s. The ordering of the W_X parameters for the ligands in the series **1.**X is $W_{N(diketiminate)} < W_{Cl} < W_{N'HR}, W_{CH_3}$ and indicates a dramatic difference in the capabilities of the two nitrogen-based ligands of perturbing the charge distribution about the nucleus of the coordinated iron site. The small values for ΔE_Q in **1.**X, as compared to the majority of high-spin ferrous complexes,

Table 3. Calculated Principal Components of $EFG^{(-)}$ in Models[a]

model[b]	V_x,[c] mm/s	V_y,[c] mm/s	V_z,[c] mm/s	W_X,[d] mm/s	$V_{z,intp}$,[e] mm/s	$W_{X,mb}$,[f] mm/s
$Fe^{III}Cl_3$	*g*	*g*	2.90[g]	0.97		0.3−1.3
			3.79[g]	1.26		
$Fe^{III}(N'H_2)_3$[h]	*g*	*g*	3.56	1.19		0.9−1.9
			4.73	1.58		
$Fe^{III}(CH_3)_3$	*g*	*g*	5.50	1.83		1.2−2.0
			6.93	2.31		
$Fe^{III}(N'H_2)_2Cl$[h]	−0.82	−2.44	3.26		3.34	
	−1.12	−3.13	4.25		4.41	
$Fe^{III}(N'H_2)_2CH_3$[h]	−2.23	−1.97	4.20		4.21	
	−2.57	−2.84	5.42		5.46	
$Fe^{III}L'Cl$[i]	0.76	−2.83	2.07	0.55		
	−1.44	−0.16	1.60	0.17		0.2−0.5
$Fe^{III}L'CH_3$[i]	−0.29	−2.15	2.45	0.87		
	−3.99	0.21	3.79	0.74		

[a] Density functional, B3LYP; basis sets, 6-31G (first line) and 6-311G (second line). Cartesian coordinates are defined in Figure 10. [b] In first five complexes, all non-hydrogen atoms are in the $x-y$ plane, and bond angle θ (Figure 10) is 120°. Crystallographic structures of cores in **1.**X for X = Cl and CH_3 were adopted for complexes listed in last two lines. The electronic spin *S* is $^5/_2$. [c] Converted from EFGs calculated in atomic units by multiplying with factor −1.719 (mm/s)/(A.U.) based on ^{57}Fe nuclear quadrupole moment $Q = 0.17$ barn. The quadrupole splitting is given by $\Delta E_Q = V_z(1 + \eta^2/3)^{1/2}$. [d] W_X values obtained by $W_X = {}^1/_3\, V_z$ for $[Fe^{III}X_3]^0$ (eq S.2); values in the last four lines are for the diketiminate nitrogens, $W_N = {}^1/_2(V_z - W_X)$, obtained by using the W_X values for $[Fe^{III}X_3]^0$. [e] Interpolated values $V_{z,intp} = 2W_{N'H_2} + W_X$, for X = Cl and CH_3, respectively, based on eq S.2. [f] W_X ranges deduced from quadrupole interactions in series **1.**X (section 4.1.3). [g] $V_x \approx V_y = -{}^1/_2\, V_z$. [h] Prime is used to distinguish N from diketiminate nitrogen. [i] Results for structure L′ in which side chains of phenyls were replaced by hydrogens and *tert*-butyls by methyls.

(28) For $\Delta E_Q > 0$, the $M_I = \pm{}^3/_2$ sublevels of the nuclear excited state are higher in energy than the $M_I = \pm{}^1/_2$ levels. Note that the sign of ΔE_Q is the reverse of the sign of the electric field gradient component with the largest magnitude. Quantum chemical codes usually provide the EFG rather than ΔE_Q and η, which may lead to confusion. To remind the reader of the sign change, we label the gradient used by Mössbauer spectroscopists as $EFG^{(-)}$. The operator for $EFG^{(-)}$ is denoted $\hat{V}$, and the largest component in magnitude of $EFG^{(-)}$ is referred to as V_{max}. Our quantities V_i correspond to $eQV_{ii}/2$ in the commonly used Hamiltonian, eq 1b, where *Q* is the nuclear quadrupole moment of ^{57}Fe and *e* is the positive unit charge.

(29) The ligand contribution includes "covalency" contributions arising from the overlap charges in the metal−ligand bonds.

indicates an extensive cancellation of positive ligand contributions and negative metal contributions to EFG$^{(-)}$ along the normal of the molecular plane.

4.2. Density Functional Calculations. 4.2.1 Electric Field Gradients. In the previous section we have introduced a scheme for parametrizing the ligand contributions to the EFG$^{(-)}$ at the iron nuclei in **1.**X which relied on the premises that (a) the EFG tensors for the ligands are additive quantities and (b) the values for the W_X parameters are transferable between the complexes. These hypotheses were tested by performing quantum chemical calculations in a number of model systems, listed in Table 3. Among the computational methodologies available to us, density functional theory (DFT) appeared to us the most appropriate technique for this purpose, as it focuses on the determination of the quantity from which the EFG is calculated, namely the charge distribution.[30,31] The calculations were carried out with the Gaussian 98 package (release A.9)[32] for charge-neutral models in the $M_S = {}^5/_2$ state and converged to solutions in which the unpaired electrons are in metal 3d-orbitals. In the absence of a sixth 3d electron, the metal contribution to the EFG$^{(-)}$ vanishes in the Fe^{3+} state. Table 3 lists the eigenvalues of the EFG$^{(-)}$ tensors computed for five trigonal models, including three models with homoleptic coordinations and two with heteroleptic ones. Assuming additivity, the V_z values for the homoleptic models were used to evaluate the W_X parameters for the three monodentate ligands (fifth column). These values were subsequently transferred to the heteroleptic models and added in order to obtain the V_z components (sixth column). The latter values and those obtained from the calculations for the heteroleptic species (fourth column) are in excellent agreement, independent of the basis set, and lend support to the notions of both additivity and transferability. Heteroleptic coordination leads to field gradient tensors with three different principal components (see Table 3). Interpolation of the in-plane components, based on the expressions for the V_x and V_y in eq S.2 of the Supporting Information, gave a somewhat less satisfactory agreement, possibly because the EFG tensors may not be quite axial along the atom−metal vectors, as assumed in section 4.1.3.

The last four lines of Table 3 contain the results for models representing the nontrigonal diketiminate coordinations in **1.**Cl and **1.**CH_3 together with estimated W_N parameters for the diketiminate nitrogens (fifth column), obtained upon transferring the W_X parameters given in the same column to these mixed-ligand species. Although transferability requires equal W_N values for the two models, these values are actually calculated to be different for the two species. We note, however, that these numbers were obtained as small differences of larger numbers and therefore are prone to any source of error. Moreover, the W values show a significant dependence on the basis set. The W_X values deduced on the basis of additivity and transferability from the computed (fifth column) and empirical (seventh column) EFG$^{(-)}$'s are in fair agreement. The computed W values corroborate the conclusion of section 4.1.3 in that the diketiminate nitrogens differ from the nitrogens in ligands of the type N′HR in their ability to perturb the charge distribution around the nucleus of the coordinated metal site. Moreover, the W parameters of N′H_2 and CH_3, for which we inferred strongly overlapping domains in the previous section, appear clearly in the order $W_{N'H_2} < W_{CH_3}$, according to the calculations.

The DFT calculations for $[Fe^{II}Cl_3]^-$ and $[Fe^{II}(CH_3)_3]^-$ (using the structures of the corresponding ferric species and the spin-unrestricted B3LYP functional and basis set 6-311G provided by the Gaussian 98 package[32]) resulted in d^6 ground states with doubly occupied z^2 orbitals and gradients $V_z = -1.09$ mm/s (chloride) and $+1.76$ mm/s (methide). These values can be used to estimate the W parameters for the Fe^{II} complexes, denoted W'. Thus, subtraction of the valence contribution $V_{Val}(z^2) = -4.9$ mm/s (computed for Fe^{II} with a z^2 ground state, using the same functional/basis set) and division by 3 yields the values $W'_{Cl} = 1.3$ mm/s and $W'_{CH_3} = 2.2$ mm/s. A comparison of these values with the W parameters for the ferric species (Table 3) shows that $W'_X \approx W_X$ and suggests that the ligand contributions are practically independent of the oxidation state of the metal ion.

4.2.2. Excited Orbital States. Analysis of the fine structure and hyperfine interactions in the ground states of the complexes in the series **1.**X allowed us to draw detailed conclusions about the nature of these states and of two low-lying excited orbital states (section 4.1). The latter states have low excitation energies and are therefore difficult to detect by means of electronic absorption spectroscopy or magnetic circular dichroism (MCD) measurements, due to overlap with vibrational overtones and the spectral limitations of the available MCD instrumention. The acquired knowledge about the ground and excited orbital states in **1.**X makes the series a suitable candidate for testing the predictive power of both DFT[30] and recently developed time-dependent (TD) DFT methodologies.[33] We used for this purpose the commonly used spin-unrestricted B3LYP functional and the basis set 6-311G provided by the Gaussian 98 package.[32] The calculations were performed on stripped versions of **1.**Cl and **1.**CH_3 in which the diketiminate ligand was simplified by replacing the side chains by hydrogens for saving computational time (structure 1). We also did calculations on more complete structures in which substitution was limited to the side chains of the phenyl rings and replacement of *tert*-butyl by methyl (structure 2) but found only minor changes in the results, using the EFG at the iron nucleus and excitation energies as indicators. The calculations were performed for $M_S = 2$ and converged to a state in which the four unpaired electrons occupy molecular orbitals with predominantly 3d character.[34] The calculations placed the two spin-paired 3d electrons of the d^6 configuration

(30) (a) Parr, R. C.; Yang, W. *Density-Functional Theory of Atoms and Molecules*; Oxford University Press: New York, 1989. (b) Dreizler, R. M.; Gross, E. K. U. *Density Functional Theory, an Approach to the Quantum Many-Body Problem*; Springer-Verlag: Berlin, 1990.

(31) Available DFT programs do not consider spin−orbit coupling, that is, an interaction shown above to be essential for understanding the electronic properties of the ground state. This precludes a direct calculation of the EFGs in **1.**X.

(32) Frisch, M. J.; Trucks, G. W.; Schlegel, H. B.; Scuseria, G. E.; Robb, M. A.; Cheeseman, J. R.; Zakrzewski, V. G.; Montgomery, J. A., Jr.; Stratmann, R. E.; Burant, J. C.; Dapprich, S.; Millam, J. M.; Daniels, A. D.; Kudin, K. N.; Strain, M. C.; Farkas, O.; Tomasi, J.; Barone, V.; Cossi, M.; Cammi, R.; Mennucci, R.; Pomelli, C.; Adamo, C.; Clifford, S.; Ochterski, J.; Petersson, G. A.; Ayala, P. Y.; Cui, Q.; Morokuma, K.; Malick, D. K.; Rabuck, A. D.; Raghavachari, K.; Foresman, J. B.; Cioslowski, J.; Ortiz, J. V.; Baboul, A. G.; Stefanov, B. B.; Liu, G.; Liashenko, A.; Piskorz, P.; Komaromi, I.; Gomperts, R.; Martin, R. L.; Fox, D. J.; Keith, T.; Al-Laham, M. A.; Peng, C. Y.; Nanayakkara, A.; Challacombe, M.; Gill, P. M. W.; Johnson, B.; Chen, W.; Wong, M. W.; Andres, J. L.; Gonzalez, C.; Head-Gordon, M.; Replogle, E. S.; Pople, J. A. *Gaussian 98*; Gaussian, Inc.: Pittsburgh, PA, 1998.

(33) (a) Gross, E. K. U.; Dobson, J. F.; Petersilka, M. In *Density Functional Theory*; Nalewajski, R. F., Ed.; Springer: Heidelberg, 1996. (b) Stratmann, R. E.; Scuseria, G. E.; Frisch, M. J. *J. Chem. Phys*, **1998,** *109*, 8218−8224. (c) Bauernschmitt, R.; Ahlrichs, R. *Chem Phys Lett.*. **1996**, *256*, 454. (d) Casida, M. E.; Jamorski, C.; Casida, K. C.; Salahub, D. R. *J. Chem. Phys.* **1998,** *108*, 4439.

(34) Gaussian 98 calculations for $LCu^{II}SCPh_3$, L = β-diketiminate, by Randall et al.[6] gave solutions in which the unpaired electron occupied a ligand orbital, at variance with experiment. No such problem arose for $LFe^{II}X$.

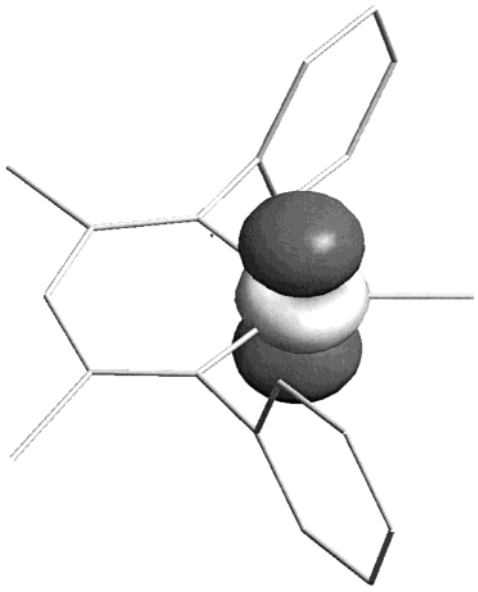

Figure 12. Contour plot of the HOMO of β-spin in **1**.Cl projected on a truncated structural model used in the DFT calculation (structure 2). β is the minority spin.

in a z^2 type orbital (Figure 12) which, in the case of **1.**CH_3, is slightly contaminated by admixture with an x^2-y^2 component. The prediction of a ground state with z^2 character is in agreement with the ground state of the crystal field that was inferred from the fine structure and hyperfine data in **1.**X. However, the comparison between computed and observed hyperfine parameters in **1.**X is a more problematic matter. These parameters are strongly affected by spin−orbit coupling (see section 4.1), and since our DFT calculations ignore magnetic interactions altogether, a meaningful comparison between theory and experiment is excluded from the beginning. The only possible exception is the Fermi contact field, which is insensitive to spin−orbit coupling in cases, like the present one, where the spin of the ground state is not affected by the coupling. The contact fields that we computed by DFT for free iron ions were in good agreement with experiment with respect to both sign $A_{fc} < 0$ and magnitude; however, calculations for the same ions placed in a coordination environment resulted in dramatically reduced contact fields, occasionally even having positive sign. This result should not misguide one into thinking that the positive hyperfine fields observed in **1.**X are caused by a sign flip of the contact field because the same behavior is also found in DFT calculations for complexes with normal (negative) contact fields. Moreover, a sign flip of the contact field would not explain the exceptionally large effective g values in **1.**X. Contact fields calculated with unrestricted Hartree−Fock theory using the same basis set are in much better agreement with experiment and show that the erroneous results for this property obtained by the DFT calculations are not related to the choice of the basis set but are rather methodological in nature.

In the following discussion the minority spin of the theoretical $M_S = 2$ state is labeled β. The calculation for **1.**CH_3 (structure 2) yields a highest occupied β spinorbital (β-HOMO) with approximately $(z^2)^\beta$ character and a sequence of virtual orbitals which appear as $(yz + L)^\beta$ (27 396), $(x^2-y^2)^\beta$ (31 126), $(xy + L)^\beta$ (34 226), $(L)^\beta$ (36 847), $(L)^\beta$ (36 977), $(L)^\beta$ (38 831), $(xz)^\beta$ (39 346), $(yz - L)^\beta$ (43 995), $(xy - L)^\beta$ (45 987), where L labels Kohn−Sham orbitals[35] with major ligand components and the numbers in parentheses are the energy eigenvalues (in cm^{-1}) of the DFT Fock matrix, taken with respect to the eigenvalue for the β-HOMO. Apart from small components, these orbitals are either of 3d type, ligand type, or 3d−ligand mixtures in roughly equal proportions. The TD-DFT output lists the excited states as linear combinations of configurations that are obtained from the Kohn−Sham monodeterminantal ground state by making single substitutions therein: $|\text{occupied} \rightarrow \text{virtual}\rangle$. With the caveats that all orbitals contain ligand components and that there are substitutions of charge-transfer type $|\text{d} \rightarrow \text{ligand}\rangle$ with small coefficients for each excited state, the lowest four excited levels obtained by TD-DFT are $|(z^2)^\beta \rightarrow (yz + L)^\beta\rangle + |(z^2)^\beta \rightarrow (yz - L)^\beta\rangle \approx |(z^2)^\beta \rightarrow (yz)^\beta\rangle$ (2108), $|(z^2)^\beta \rightarrow (x^2-y^2)^\beta\rangle$ (6179), $|(z^2)^\beta \rightarrow (xz)^\beta\rangle$ (6729), $|(z^2)^\beta \rightarrow (xy + L)^\beta\rangle + |(z^2)^\beta \rightarrow (xy - L)^\beta\rangle \approx |(z^2)^\beta \rightarrow (xy)^\beta\rangle$ (12 535). In the case of the yz and xy excitations, the configuration interaction leads to an "unmixing" of the transitions into $\text{d} \rightarrow \text{d}'$ and charge transfer, and it is therefore incorrect to identify the excited states with the (highly covalent) virtual Kohn−Sham orbitals. Such an identification is also improper from an energetic point of view, as can be seen by comparing the orbital energies with the TD-DFT excitation energies (in parentheses), the former exceeding the latter by as much as a factor of 3. The lowest four excitations are metal-based and involve the standard Cartesian 3d-orbitals, thus corroborating the analysis given in section 4.1. The TD-DFT calculation correctly predicts the ordering $\epsilon_{z^2} < \epsilon_{yz} < \epsilon_{xz}$ but fails to reproduce the accidental near degeneracy of z^2 and yz; the computed orbital splitting (2108 cm^{-1}) gives a too-small effective g value (9.1, using eqs 5a,b) that lies far outside the error margin for this quantity (Table 1). The calculated $xz-yz$ splitting is 4071 cm^{-1} and close to the value estimated from the analysis of zero-field splitting Δ in section 4.1.2. The TD-DFT results for **1.**Cl are similar to those for **1.**CH_3, apart from the x^2-y^2 excitation energy, which is lower by about 1700 cm^{-1}. The latter result confirms that Cl^- is a weaker σ donor than CH_3^-.

Oldfield and co-workers have shown that DFT is a reliable tool for predicting the electric hyperfine parameters in a large number of metalloporphyrins.[36] The good agreement between the calculated and empirical W_X parameters for **1.**X confirms the utility of DFT. The complexes **1.**X differ from the earlier studied macrocyclic species in that there is a low-lying excited state which affects the EFG through admixture by spin−orbit coupling. This complication makes the ab initio prediction of the quadrupole splittings in systems such as **1.**X virtually impossible. For the spin−orbit effect on the EFG to be significant, the energy level of the admixing state should lie within $\sim 5|\lambda|$ from the ground level (see Figure S.1). As the relevant energy gaps amount to only a few hundred wavenumbers, a reliable prediction of the quadrupole interactions in **1.**X requires the TD-DFT calculation for the excitation energies to be accurate within 100 cm^{-1}, exceeding the currently available computational precision by at least 1 order of magnitude.

4.2.3. Isomer Shifts of 1.X. A comparison of the isomer shifts observed for **1.**X (Table 1) with those for complexes with coordination number greater than 3 indicate that these values follow the rule that δ decreases with decreasing coordination

(35) Kohn, W.; Sham, L. *Phys. Rev. A* **1965,** *140*, 1133.
(36) Havlin, R. H.; Godbout, N.; Salzmann, R.; Wojdelski, M.; Arnold, W.; Schulz, C. E.; Oldfield, E. *J. Am. Chem. Soc.* **1998**, *120*, 3144−3151.

number.[37] Moreover, Table 1 reveals remarkably large changes in the isomer shift upon replacements at a single ligand position, X. In comparing the tabulated numbers, it is to be noted that a smaller δ value is associated with a higher electron density at the ^{57}Fe nucleus. We tested this prediction by means of DFT calculations on the model complexes $[Fe^{II}L'Cl]^0$ and $[Fe^{II}L'(CH_3)_3]^0$, where L′ is defined as in Table 3, and indeed found that this trend is corroborated by the values for the electron density, $\rho(0)$, at the iron sites. Thus, $\rho(0)$ in **1.**CH_3 is calculated to be greater than in **1.**Cl by $\Delta\rho(0) = 0.7a_o^{-3}$ (a_o = 1 Bohr). The increase in the density corresponds to a decrease in the isomer shift, $\Delta\delta = -0.26$ mm s^{-1} (Table 1), which leads to a slope $\alpha = \Delta\delta/\Delta\rho(0) \approx -0.37$ mm s^{-1} a_o^3, which is in accordance with earlier estimates of this quantity.[38]

4.3. Trigonal Sites in Fe−Mo Cofactor in Nitrogenase. Finally, we wish to comment on some spectroscopic properties that have puzzled us for over 20 years. The Mössbauer spectra of the $MoFe_7S_9$ cluster in the $S = {}^3/_2$ state M^N (see ref 8) yield one quadrupole doublet with $\Delta E_Q \approx 0.7$ mm/s and $\delta = 0.41$ mm/s at 100 K, where fast spin relaxation prevails. Six of the seven iron sites of the cofactor cluster have a nearly trigonal sulfido coordination, and thus it is not surprising that they have the same, or nearly the same, quadrupole splittings. However, the magnitude of the quadrupole splitting was substantially smaller than anticipated for a cluster in which at least four[8d] or perhaps six[39] iron sites are thought to be ferrous (N.B.: The majority of the $S = 2$, Fe^{II} complexes has ΔE_Q values between 2.5 and 3.3 mm/s).[14] Nearly the same quadrupole splitting, $\Delta E_Q = 0.81$ mm/s, has been reported by Power and collaborators for the high-spin Fe^{II} complex $[Fe(SC_6H_2\text{-}2,4,6\text{-}t\text{-}Bu_3)_3]^-$ in which a trigonal thiolate coordination is enforced by using sterically encumbered ligands.[3h] The analysis described here and the data cited in the Supporting Information suggest that there is an extensive cancellation of positive and negative contributions to the $EFG^{(-)}$ along the normal of the molecular plane, leading to unusually small quadrupole splittings for these three-coordinate ferrous species. We appreciate now that three-coordinate Fe^{II} complexes may have small isomer shifts (the Power complex has $\delta = 0.57$ mm/s at 4.2 K) and unusually small quadrupole splittings, resulting from substantial ligand contributions in these planar environments. Without this recognition, it was difficult to assign oxidation states to the "trigonal" iron sites of the cofactor. In fact, until suitable ferric complexes with trigonal sulfido/thiolato coordination become available, caution is advised in assigning oxidation states to three-coordinate sites in multinuclear complexes.

(37) Kurtz, D. M., Jr. *Chem. Rev.* **1990,** *90,* 585.
(38) Bominaar, E. L.; Guillin, J.; Sawaryn, A.; Trautwein, A. X. *Phys. Rev. B* **1989**, *39*, 72−79.
(39) True, A. E.; Nelson, M. J.; Venters, R. A.; Orme-Johnson, W. H.; Hoffman, B. M. *J. Am. Chem. Soc.* **1998**, *110,* 1935−1943.

Acknowledgment. P.L.H. thanks Rene Lachicotte for assistance with crystallography and Kevin Mooney for measuring SQUID data. We thank Thomas Cundari for sharing the results of calculations that were not included here. We thank Vladislav Vrajmasu and Sebastian Stoian for assistance in the project. P.L.H. acknowledges funding from the University of Rochester. This research was supported by National Science Foundation Grant MCD-9416224 (E.M.) and National Institute of Health Grant GM-22701 (E.M.).

Supporting Information Available: Sections S.1 and S.2, Table S.1, and Figures S.1−4 describing the analysis of the electric hyperfine interactions; Tables S.2−7 and Figure S.5 containing the crystallographic data for complex **1.**CH_3 (PDF). This material is available free of charge via the Internet at http://pubs.acs.org.

JA012327L